

## RESEARCH ARTICLE

10.1002/2017JD026890

## Key Points:

- Stratospheric variability exerts a stronger influence on ozone intrusions than tropospheric jet variability
- Ozone intrusion frequency is more related to wave breaking frequency than it is to teleconnection patterns
- The strength of the winter stratospheric Northern Annular Mode is indicative of spring ozone intrusion strength

## Correspondence to:

J. R. Albers,  
john.albers@noaa.gov

## Citation:

Albers, J. R., Perlwitz, J., Butler, A. H., Birner, T., Kiladis, G. N., Lawrence, Z. D., ... Dias, J. (2018). Mechanisms governing interannual variability of stratosphere-to-troposphere ozone transport. *Journal of Geophysical Research: Atmospheres*, 123, 234–260. <https://doi.org/10.1002/2017JD026890>


Received 3 APR 2017

Accepted 3 DEC 2017

Accepted article online 7 DEC 2017

Published online 12 JAN 2018

# Mechanisms Governing Interannual Variability of Stratosphere-to-Troposphere Ozone Transport

John R. Albers<sup>1,2</sup> , Judith Perlwitz<sup>1,2</sup> , Amy H. Butler<sup>1,3</sup> , Thomas Birner<sup>4</sup> , George N. Kiladis<sup>2</sup>, Zachary D. Lawrence<sup>5</sup> , Gloria L. Manney<sup>5,6</sup> , Andrew O. Langford<sup>3</sup> , and Juliana Dias<sup>1,2</sup> 

<sup>1</sup>Cooperative Institute for Research in the Environmental Sciences, University of Colorado Boulder, Boulder, CO, USA,

<sup>2</sup>Physical Sciences Division, NOAA Earth System Research Laboratory, Boulder, CO, USA, <sup>3</sup>Chemical Sciences Division,

NOAA Earth System Research Laboratory, Boulder, CO, USA, <sup>4</sup>Department of Atmospheric Science, Colorado State

University, Fort Collins, CO, USA, <sup>5</sup>Department of Physics, New Mexico Institute of Mining and Technology, Socorro, NM,

USA, <sup>6</sup>NorthWest Research Associates, Socorro, NM, USA

**Abstract** Factors governing the strength and frequency of stratospheric ozone intrusions over the Pacific-North American region are considered for their role in modulating tropospheric ozone on interannual timescales. The strength of the association between two major modes of climate variability—the El Niño–Southern Oscillation (ENSO) and the Northern Annular Mode (NAM)—and the amount of ozone contained in stratospheric intrusions are tested in the context of two mechanisms that modulate stratosphere-to-troposphere transport (STT) of ozone: (StratVarO<sub>3</sub>) the winter season buildup of ozone abundances in the lowermost stratosphere (LMS) and (JetVar) Pacific jet and wave breaking variability during spring. In essence, StratVarO<sub>3</sub> corresponds to variability in the amount of ozone per intrusion, while JetVar governs the frequency of intrusions. The resulting analysis, based on two different reanalysis products, suggests that StratVarO<sub>3</sub> is more important than JetVar for driving interannual variations in STT of ozone over the Pacific-North American region. In particular, the abundance of ozone in the LMS at the end of winter is shown to be a robust indicator of the amount of ozone that will be contained in stratospheric intrusions during the ensuing spring. Additionally, it is shown that the overall strength of the winter season stratospheric NAM is a useful predictor of ozone intrusion strength. The results also suggest a nuanced relationship between the phase of ENSO and STT of ozone. While ENSO-related jet variability is associated with STT variability, it is wave breaking frequency rather than typical ENSO teleconnection patterns that is responsible for the ENSO-STT relationship.

## 1. Introduction

Determining the concentrations of ozone that would be present in the absence of any anthropogenic ozone precursor emissions from North America—the North American Background (NAB)—continues to be a vexing problem in part because of difficulties associated with accurately accounting for nonlocal sources of ozone. One significant nonlocal source of tropospheric ozone over western North America is downward transport via stratospheric intrusions (Cooper et al., 2005; Langford et al., 2009, 2012, 2015, 2016; Lefohn et al., 2011; Lin et al., 2015; Terao et al., 2008).

Most deep stratospheric intrusions are created through the formation of tropopause folds that result from Rossby wave breaking. Irreversible stratosphere-to-troposphere transport (STT) occurs when Rossby wave filaments (stratospheric intrusions) are eroded due to some combination of turbulent mixing and diabatically induced cross-isentropic circulations (Hoerling et al., 1993; Langford & Reid, 1998; Shapiro, 1980). In the western United States, STT of ozone due to stratospheric intrusions peaks in late spring (Elbern et al., 1998; James et al., 2003; Lefohn et al., 2011; Lin et al., 2012; Olsen et al., 2013; Škerlak et al., 2014) along isentropes near to the 330 K surface (Škerlak et al., 2015).

For localized regions such as North America, previous research (see references below) suggests that a significant fraction of interannual variations in STT of ozone is governed by variability in the amount of stratospheric ozone that is available for intrusions to mix downward (StratVarO<sub>3</sub>) and the frequency and geographic

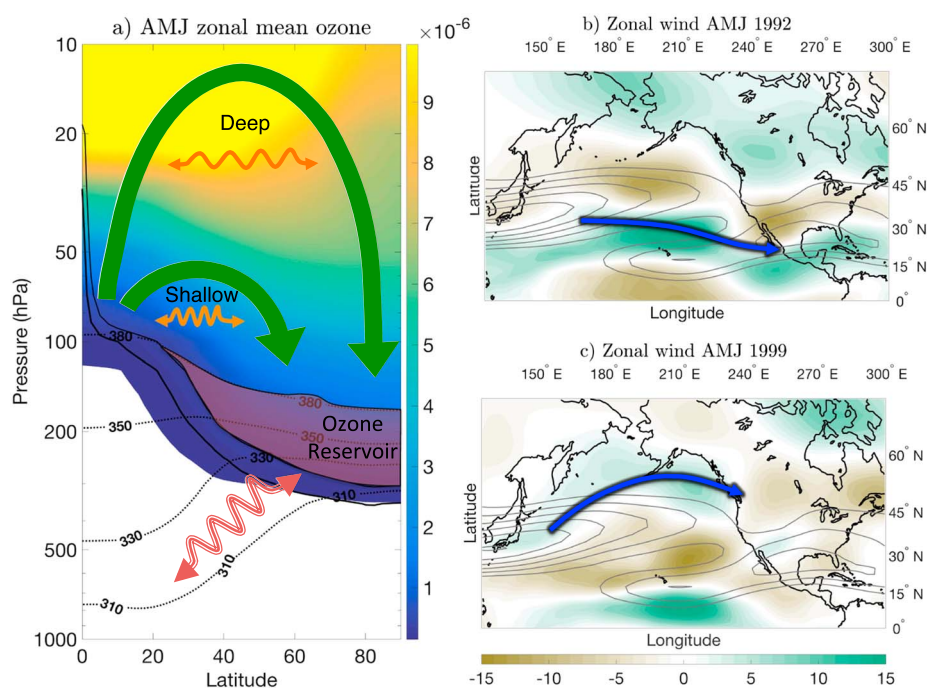


**Figure 1.** Schematic depiction of the mechanisms that contribute to the interannual variability of spring season STT of ozone over the Pacific-North American region: (a) winter season stratosphere-controlled buildup of ozone in the lower stratospheric reservoir that serves as the source of ozone available for STT (StratVarO<sub>3</sub>) and (b, c) north-south shifts in Pacific Basin waveguide/teleconnection patterns that govern the frequency and location of stratospheric intrusions (JetVar). In Figure 1a, the background colored contours show the ERA-Interim April–June (AMJ) (1979–2015) zonal mean ozone distribution (units of mass mixing ratio), the black dashed lines denote AMJ zonal mean potential temperature surfaces (K), the two black solid lines denote 2 PVU (PV unit) and 4 PVU isosurfaces that are common measures of the dynamical tropopause, the green thick arrows denote the deep and shallow branches of the BDC, the orange horizontal wavy arrows denote quasi-isentropic mixing, the purple opaque region between the dynamical tropopause and the 380 K isentropic surface denotes the lower stratospheric ozone reservoir, and the pink wavy arrow denotes stratosphere-troposphere exchange associated with stratospheric intrusions. Figures 1b and 1c show April–May time average ERA-Interim zonal winds (gray contours; unit of m s<sup>-1</sup>) and zonal wind anomalies (filled contours; unit of m s<sup>-1</sup>) on the 350 K isentropic surface for years with southward (Figure 1b, 1992) and northward (Figure 1c, 1999) shifts in the zonal jet that are consistent with typical El Niño and La Niña jet shifts, respectively, which we depict schematically by the blue thick arrows.

distribution of the intrusion events themselves (JetVar). StratVarO<sub>3</sub> is controlled by the strength of the stratospheric circulation during the winter season, while JetVar is controlled, at least in part, by upper tropospheric-lower stratospheric (UTLS) jet stream variability during the spring intrusion season. Figure 1 and the list of mechanisms below summarize the physical processes that govern StratVarO<sub>3</sub> and JetVar.

1. Stratospheric ozone variability—StratVarO<sub>3</sub>. The extratropical lowermost stratosphere (LMS) is typically defined as the region between the dynamical tropopause (defined here as the region between the 2 potential vorticity unit (PVU) (PV unit  $\equiv 10^{-6} \text{ K m}^2 \text{ kg}^{-1} \text{ s}^{-1}$ ) and 4 PVU surfaces) and the 380 K isentropic surface (Holton et al., 1995; Hoskins, 1991). Ozone variability in this region modulates STT of ozone (e.g., Figure 5 of Liang et al., 2009) because it is this thin layer that intrusions are able to tap into when mixing ozone downward into the troposphere (Gettelman et al., 2011; Holton et al., 1995; Shapiro, 1980). The richness of this spring ozone “reservoir” (Figure 1a) is controlled by the strength of the Brewer-Dobson circulation (BDC)—which includes both the residual circulation (green arrows in Figure 1a) and quasi-horizontal mixing (orange wavy arrows in Figure 1a)—and to a lesser extent, heterogeneous chemical loss when the lower stratosphere is particularly cold in springtime (e.g., Manney et al., 2011). Because of the meridional gradient of ozone in the upper versus lower stratosphere (Figure 1a), the deep branch of the BDC increases the amount of ozone in the reservoir, while the shallow branch of the BDC generally diminishes the amount of ozone in the reservoir (Bönisch et al., 2009; Butchart, 2014; Hegglin & Shepherd, 2007; Neu et al., 2014; Pan et al., 1997; Rood et al., 2000; Shepherd, 2007). The BDC is a wave-driven phenomenon that is strongest in the winter and weak in the summer; this means that the amount of ozone contained in the

reservoir at the beginning of spring should in principle be at least partly governed by the strength of stratospheric wave driving during the prior winter season along the deep versus shallow branches of the BDC (see section A1 for further BDC and stratospheric reservoir background).

2. Jet variability—JetVar. North Pacific jet variability, which incorporates aspects of the subtropical and the polar front jets, modulates the frequency and location of intrusions over the western United States in late spring. This mechanism provides a pathway for internal atmospheric variability and modes of low-frequency variability (e.g., the El Niño–Southern Oscillation) to govern North American intrusions (e.g., Lin et al., 2015). For example, Figures 1b and 1c show April–May time mean winds for the Pacific jet on the 350 K isentropic surface with jet stream patterns that preferentially direct Rossby waves either southward toward Central America (Figure 1b, 1992 El Niño) or northward toward the western United States (Figure 1c, 1999 La Niña), which are typical patterns representative of El Niño–Southern Oscillation (ENSO) jet shifts (e.g., Ji et al., 2016; Shapiro et al., 2001).

These two mechanisms provide the means for climate variability on interannual to decadal timescales—in both the stratosphere and troposphere—to modulate STT of ozone. For example, changes in the strength of stratospheric planetary wave driving, which modulates the BDC and thus extratropical ozone abundances (StratVarO<sub>3</sub>), can be influenced by major modes of extratropical climate variability including ENSO, the stratospheric portion of the Northern Annular Mode (NAM), and the quasi-biennial oscillation (QBO) (e.g., García-Herrera et al., 2006; Hsu & Prather, 2009; Kiesewetter et al., 2010; Zhang et al., 2017). Likewise, ENSO—though typically weak during spring and summer—and the UTLS portion of the NAM are associated with shifts in Pacific wave breaking patterns and thus STT of ozone via JetVar. While previous research has connected low-frequency variability to tropospheric ozone variability, there is still a large degree of uncertainty regarding which of the mechanisms (StratVarO<sub>3</sub> or JetVar) is the dominant factor controlling STT of ozone over North America on interannual timescales.

In terms of StratVarO<sub>3</sub>, observational data and model-based studies have shown that regional (Hess & Zbinden, 2013) and global (Hess et al., 2015; Neu et al., 2014; Olsen et al., 2013; Zeng & Pyle, 2005) midlatitude tropospheric ozone variability at 500 hPa is strongly correlated with lower stratospheric ozone abundances on interannual timescales. While some of these studies (e.g., Hess et al., 2015; Neu et al., 2014) attribute this correlation to year-to-year fluctuations in the BDC, Hsu and Prather (2014) find a more nuanced relationship between the BDC and STT of ozone. Moreover, of the studies that find a connection between the BDC and STT of ozone, there remains uncertainty regarding the relative importance of the different types of low-frequency variability for driving the BDC-driven fluctuations in STT of ozone. Zeng and Pyle (2005) and Neu et al. (2014) suggest that the warm phase of ENSO and the easterly phase of the QBO lead to higher than normal STT of ozone, while Hsu and Prather (2009) and Hess et al. (2015) find very little relationship between ENSO and STT of ozone. Kiesewetter et al. (2010) demonstrated that stratospheric NAM anomalies, which are closely tied to variations in the BDC, are followed by ozone anomalies that slowly descend from the upper to lower stratosphere on monthly timescales, yet Hsu and Prather (2009) find a weak relationship between the Arctic Oscillation and STT of ozone.

However, other studies suggest that changes in STT of ozone are not associated with variability in the richness of the lower stratospheric ozone reservoir but rather are primarily due to Pacific jet variability (i.e., JetVar). Again, there is uncertainty regarding the role of ENSO. Langford et al. (1998) and Langford (1999) suggest that the warm phase of ENSO and the associated Pacific subtropical jet shift cause an increase in shallow STT of ozone into the midtroposphere over western North America that is not associated with wave breaking. Voulgarakis et al. (2011) also suggest that El Niño-related changes in tropopause level dynamics—not stratospheric variability—lead to an increase in STT of ozone. In contrast, Lin et al. (2015) and Olsen et al. (2016) suggest that it is the cold phase of ENSO that is more strongly associated with increased deep STT of ozone over western North America. Lamarque and Hess (2004) and Thouret et al. (2006) find that a significant portion—up to 50%—of spring tropospheric ozone variability over North America is associated with NAM-related tropospheric height variability (see also, Ambaum & Hoskins, 2002). Though the NAM-centered studies do not explicitly demonstrate a causal mechanism, they speculate that the anomalies are associated with the north-south meandering of storm track patterns (e.g., Thompson & Wallace, 1998).

With these differing sets of results in mind, the focus of this study is to examine the relative importance of StratVarO<sub>3</sub> and JetVar for modulating the amount of ozone that is contained in spring season stratospheric intrusions over the Pacific-North American region. By focusing on specific mechanisms of STT of ozone and

their relationship to modes of climate variability such as ENSO and the NAM, we seek to clarify what conditions matter most for driving variations in spring STT of ozone.

This paper yields three primary results: first, we find that StratVarO<sub>3</sub> is more important than JetVar for driving interannual variations in STT of ozone; second, the stratospheric portion of the NAM is significantly correlated with STT of ozone via StratVarO<sub>3</sub>, while ENSO has a weak, reanalysis-dependent correlation to STT of ozone via both StratVarO<sub>3</sub> and JetVar; and third, the connection between JetVar and STT of ozone is more consistent with jet variability related to Pacific wave breaking frequency than it is with typical ENSO teleconnection patterns.

Section 2 summarizes our methods for measuring the stratospheric ozone reservoir, the amount of ozone contained in stratospheric intrusions, and defines the various reservoir, intrusion, and low-frequency variability indices we use in our analysis. Section 3 then evaluates the relative importance of mechanisms StratVarO<sub>3</sub> and JetVar in the context of the NAM, ENSO, and internal variability in both the stratosphere and troposphere. Summary and conclusions are provided in section 4.

## 2. Data and Indices

We use ERA-Interim (1979–2015) (Dee et al., 2011) and MERRA-2 (1980–2015) (Bosilovich et al., 2015; Global Modeling and Assimilation Office (GMAO), 2015; Gelaro et al., 2017) reanalyses for ozone. EOS Aura Microwave Limb Sounder (MLS) (2005–2015) (Livesey et al., 2017) ozone is used to evaluate the accuracy of the reanalyses ozone distributions in the LMS (section A1). ERA-Interim and MERRA-2 data were first interpolated from their native model level grids to isentropic levels, and then, to ensure that the comparison of our reservoir and intrusion calculations was consistent, we regridded both data sets to a 2.5° Gaussian grid with 6-hourly temporal resolution. While there are known issues with ozone in reanalyses related to inadequate model chemistry and data assimilation discontinuities associated with satellite changes (e.g., Dragani, 2011), our comparison of ERA-Interim, MERRA-2, and MLS ozone (see Appendix A) and a recent assessment of MERRA-2 ozone in the UTLS (Wargan et al., 2017) suggest that reanalyses should be adequate for estimating March lower stratospheric ozone abundances and the amount of ozone contained in stratospheric intrusions. We did not attempt to detrend any of the ozone time series or account for any data discontinuities in either reanalysis with one exception. When computing various ERA-Interim ozone quantities, we noticed a significant—and unphysical—discontinuity in the time series between 2002 and 2003 (e.g., Figure 19 of Škerlak et al., 2014). To address this issue, we adjusted the ozone reservoir and ozone intrusion mass indices that we calculated using ERA-Interim so that the pre-2002 and post-2003 mean and standard deviations (STDs) were equal.

Recent work comparing the interannual variability of stratospheric winds (Long et al., 2017) and annular mode structures (Kang et al., 2014; Martineau & Son, 2010) has shown that modern reanalyses—including MERRA-2 and ERA-Interim—agree extremely well. For example, time series of the Arctic Oscillation for MERRA-2 and ERA-Interim have a correlation of 0.99 (Kang et al., 2014). Thus, for calculations involving the NAM and jet variability, we simply use ERA-Interim dynamic variables. Table 1 provides a listing and brief description of the indices used in the results presented in section 3, while sections 2.1–2.3 describe in detail how each of these indices is calculated.

### 2.1. Spring Ozone Reservoir Proxy

Our analysis in section 3 requires an index that quantifies the amount of ozone contained in the LMS reservoir relevant to the Pacific and North American regions. The ozone reservoir index (RzvrMass) is calculated by summing up the amount of ozone contained in a fixed “box” between 150° and 290°E and 55–60°N on the 350 K isentropic surface and then removing the 1979–2015 mean of ozone inside the box to create an anomaly time series. We chose this particular box because the 350 K surface is roughly in the middle (vertically) of the ozone reservoir (Figure 1a) and spans the portion of the midlatitude Pacific–North American region that is the focus of this study. ERA-Interim, MERRA-2, and MLS agree quite well in terms of interannual ozone variability within the LMS, which we discuss in detail (including a visual depiction of our RzvrMass box boundaries) in section A1.

We did explore other latitude and longitude RzvrMass box boundaries by testing how the correlation between ozone intrusion mass (defined in section 2.2) and RzvrMass was sensitive to the location and size of the RzvrMass box. Specifically, the RzvrMass box was moved poleward and equatorward in combination with extending the box to include all longitudes. We found that 55–60°N produced the highest RzvrMass–ozone intrusion mass correlations, while moving the box poleward or equatorward and extending it to include all

**Table 1**

List of Indices (Left Column) Used in Section 3 and a Brief Description of What They Represent (Right Column)

Index	Description
RzvrMass	Proxy for measuring the amount of ozone contained in the lowermost stratospheric reservoir. The boundaries of RzvrMass are 150°–290°E and 55°–60°N on the 350 K isentropic surface.
IntrMass	Amount of ozone contained in intrusions between AMJ for North America or the Pacific Basin and North America measured on the 330 K isentropic surface along 40°N.
NAM <sup>Strat</sup> <sub>winter</sub>	Winter season time-summed stratospheric NAM index pressure weight averaged between 5 and 10 hPa. The time-summing period is varied from 1 October to 31 March to 1 March 1 to 31 March 31.
NAM <sup>UTLS</sup> <sub>spring</sub>	Spring season time-summed (AMJ) UTLS NAM index on the 200 hPa pressure surface.
ENSO <sub>winter</sub> , ENSO <sub>spring</sub>	Extended winter (October–March) and late spring (April–May), respectively, time-summed ENSO index (ONI).

*Note.* All indices have one value for each year in the reanalyses data record (1979–2015), except for NAM<sup>Strat</sup><sub>winter</sub>, which has values for every day between 1 October and 31 March of every year (1979–2015). RzvrMass and IntrMass are each calculated twice, once using ERA-Interim and once using MERRA-2; the NAM indices are calculated using ERA-Interim, and the ENSO indices are calculated using the NOAA Oceanic Niño Index (ONI).

longitudes decreased the correlations. Nevertheless, all boxes similar to the one presented here typically had correlations that remained significant and yielded qualitatively similar results to those presented in section 3. We discuss the validity of using reanalyses data by comparing ozone from Aura MLS to the two reanalyses for 2005–2015 in section A1.

## 2.2. Intrusion Identification and Intrusion Indices

One of the key mechanistic arguments that we wish to test is that sign and strength of March stratospheric ozone reservoir anomalies (RzvrMass) strongly govern how much ozone is contained within stratospheric intrusions in the ensuing months of April–June (AMJ). Stratospheric intrusions are detected using the object-oriented algorithm of Albers et al. (2016), which identifies intrusion filaments based on a space-time-magnitude criterion and is similar to the “crossover” method employed in the ozone STT study of Morgenstern and Carver (2001). Our algorithm can be applied to any variable provided that there is a strong gradient of that variable across the dynamical tropopause; this enables us to calculate the mass of ozone within intrusions using either potential vorticity (PV) or ozone itself.

In all of our results we apply our algorithm on the 330 K surface along 40°N. Choosing the 330 K surface and 40°N for our calculations was done for two related reasons. First, the slope of the 330 K surface (Figure 1a) taps into the stratospheric reservoir while still encroaching into the troposphere over the continental United States. In contrast, surfaces above this level (e.g., 350 K, Figure 1a) are typically associated with more purely isentropic mixing into the subtropics (Albers et al., 2016), while surfaces far below 330 K (e.g., 310 K, Figure 1a) do not tap into the ozone reservoir at all. Second, 40°N was chosen because it is in the center of the region of interest in the context of NAB ozone concentrations (i.e., ozone levels between 30° and 50°N). Nevertheless, because the 315 K surface taps into the lowermost reaches of the reservoir and encroaches more deeply into the troposphere compared to the 330 K surface, we did run several tests using the 315 K level (see details below).

Our methods for calculating the amount of ozone associated with individual intrusions are understood most easily in the context of a canonical event. PV on the 330 K isentrope for 4 May 1998 (Figure 2a) shows a Rossby wave breaking event unfolding over the western coast of the United States. Modified PV (Lait, 1994; Müller & Günther, 2003) and ozone cross sections (Figures 2b and 2c) corresponding to the gray line at 245°E in Figure 2a show a tongue of high PV/ozone extending downward from the UTLS to nearly 900 hPa; the upward and downward deformed tropospheric and stratospheric potential temperature surfaces, respectively, in Figure 2c are indicative of the cyclonic disturbance that is embedded in the PV filament (Thorpe, 1986). Figure 2d shows vertical profiles of ozone measured by the NOAA lidar system at Fritz Peak Observatory



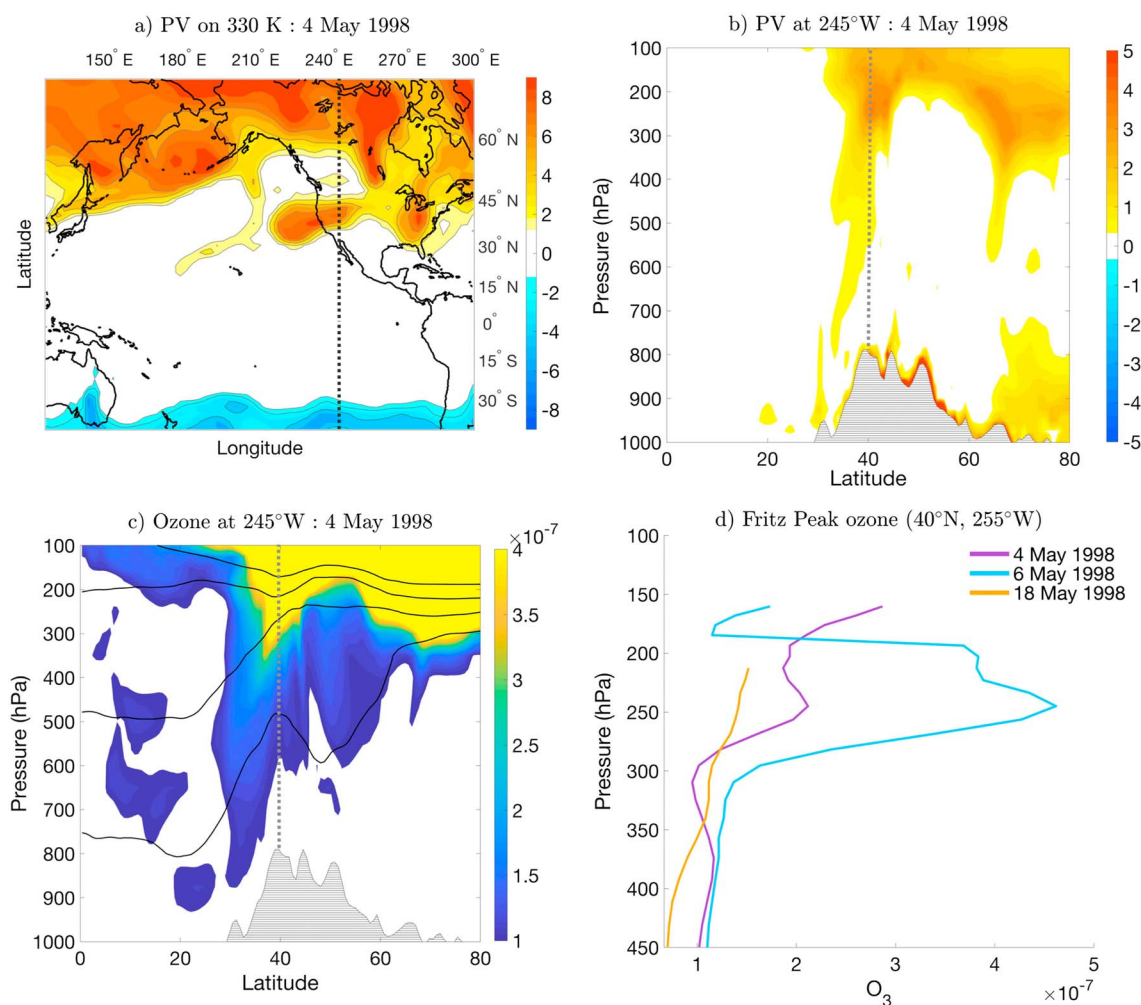


**Figure 2.** (a) PV on the 330 K isentropic surface for 4 May 1998. In Figure 2a the black vertical dotted line at 245°E corresponds to the longitude of the latitude-height cross sections of PV and ozone shown in (Figure 2b) and (Figure 2c), respectively. Latitude-height cross sections on 4 May 1998 for (b) PV and (c) ozone, where regions at or below the Earth's surface are masked with thin horizontal lines and a black outline. In Figures 2b and 2c, the gray vertical dotted lines at 40°N correspond to the (d) latitude of the Fritz Peak lidar profiles. In Figure 2c, the black solid lines correspond to the 310, 330, 350, and 370 K (bottom to top) potential temperature surfaces. Ozone lidar profiles for 4, 6, and 18 May 1998 at the Fritz Peak, Colorado observatory, where the colors of the lines correspond to the dates and locations of equivalently colored dot markers in Figure 3d. Figures 3a–3c use ERA-Interim data and have units of PVU; Figure 3d is NOAA Fritz Peak Observatory data, and the units are mass mixing ratio.

(Proffitt & Langford, 1997), which is located slightly to the east of the cross sections shown in Figures 2b and 2c (the vertical dotted lines overlaying Figures 2b and 2c denote the latitude of the Fritz Peak Observatory). The lidar ozone profiles confirm the presence of anomalously high ozone as the intrusion passes overhead. As the PV disturbance amplifies, overturns, and is advected eastward in the background flow, a “fingerprint” of PV and ozone associated with its filamentary structure is traced out in longitude time space (Figure 3).

Figure 3 shows contours of PV (gray shading in Figures 3a and 3b) and ozone (gray shading in Figures 3c and 3d) with red and green contours enclosing longitude-time traces of intrusion filaments detected by our algorithm when applied individually to PV and ozone, respectively. In order to be detected by our algorithm, PV or ozone traces must remain at least 5° longitude wide, last at least 12 h, and the whole enclosed region must exceed  $5.25 \times 10^{-7}$  PV units ( $\text{PVU} \equiv 10^{-6} \text{ K m}^2 \text{ kg}^{-1} \text{ s}^{-1}$ ) when applied to PV and  $5.1 \times 10^{-7}$  mass mixing ratio when applied to ozone. The  $5.1 \times 10^{-7}$  mass mixing ratio value was chosen as our ozone threshold because it is the boundary of the 95th percentile of ERA-Interim AMJ ozone mass mixing ratio values on 330 K along 40°N over the Pacific-North American region; for MERRA-2, the 95th percentile boundary is  $4.6 \times 10^{-7}$ , so we use this threshold when applying our algorithm to this data set. While the algorithm cannot differentiate

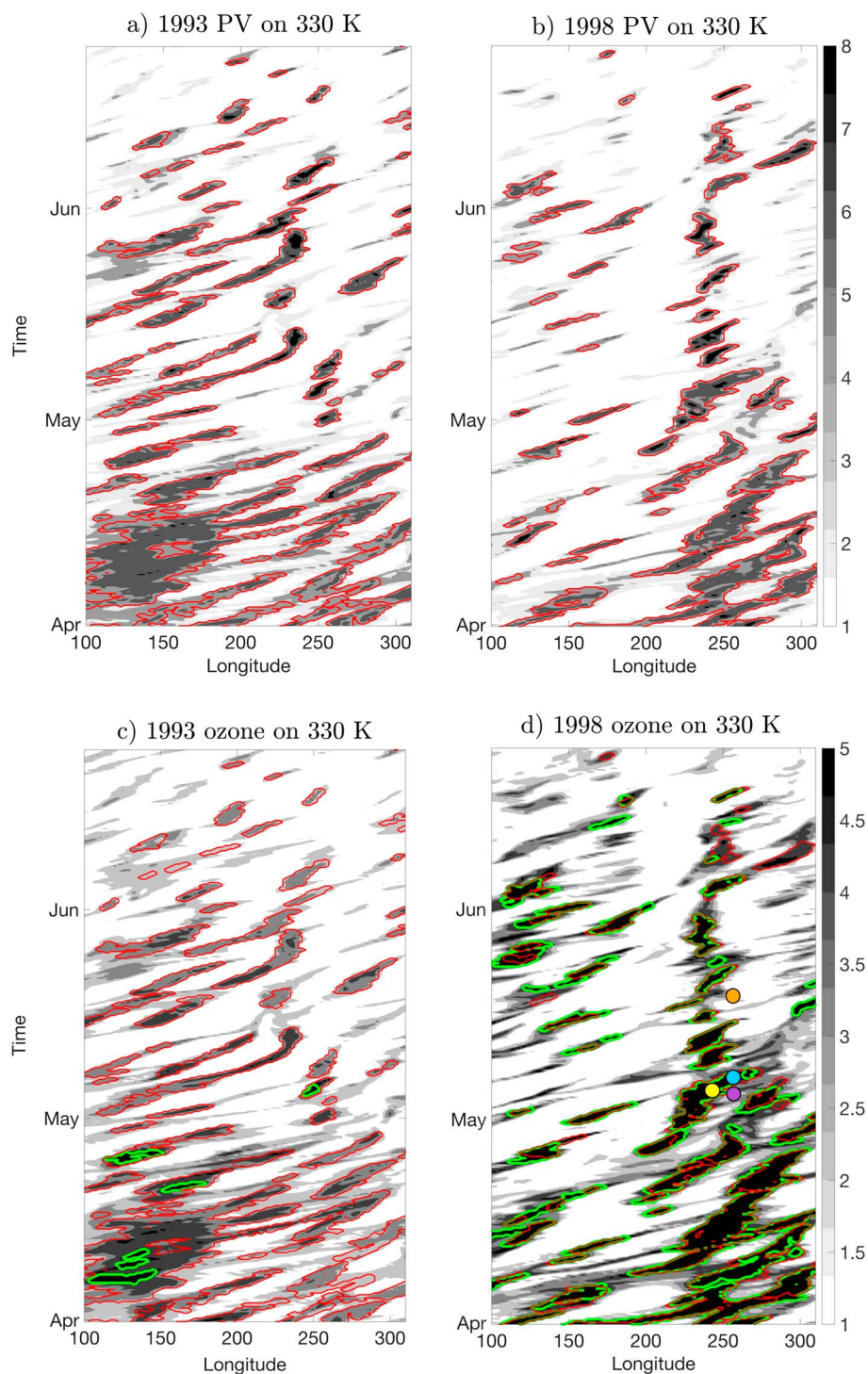


**Figure 3.** Longitude-time plots on the 330 K isentropic surface at 40°N of (a, b) PV and (c, d) ozone. In all figures, the red and green contours denote intrusion trace outlines when the intrusion detection algorithm is applied to PV and ozone, respectively, per the criterion described in section 2.2. In Figure 3d, the yellow dot corresponds to the date (4 May 1998) and longitude (245°E) of the PV and ozone cross sections in Figures 2b and 2c, respectively, and the purple, blue, and orange dots correspond to the times (4, 6, and 18 May 1998, respectively) and longitude (255°E) of the ozone lidar profiles in Figure 2d. Units for Figures 3a and 3b are PVU, and units for Figures 3c and 3d are  $10^{-7}$  mass mixing ratio; all data are ERA-Interim.

between reversible and irreversible deformations of the dynamical tropopause, a visual inspection of many individual cases suggests that when the above relatively strict threshold criteria are applied along 40°N on the 330 K isentropic surface, the algorithm correctly identifies intrusions while minimizing “false positives” associated with small undulations in the dynamical tropopause (other thresholds were tested and all reasonable values qualitatively reproduce our results). Still, it should be noted that our algorithm does not formally measure irreversible STT ozone transport.

Evidence showing that the traces identified by our algorithm are indicative of stratospheric intrusions can be seen by noting that the time period marked by the yellow dot in Figure 3d is consistent with the PV and ozone cross sections at the same time and location (c.f. Figures 2b and 2c), and the time periods marked by the purple, blue, and orange dots in Figure 3d are consistent with the ozone lidar profiles (Figure 2d) for the time periods just before intrusion passage (purple profile), during intrusion passage (blue profile), and after passage (orange profile), respectively. The clear correspondence between the PV (red) and ozone (green) contours in Figure 3d reflects the high correlation between ozone and PV along the dynamical tropopause. While all ozone anomalies detected by our algorithm are clearly associated with PV anomalies, not all PV anomalies contain ozone-rich air (c.f. Figures 3c and 3d); this result hints at the strong governing effect that the stratospheric ozone reservoir exerts on the amount of ozone contained in intrusions (section 3).

We estimate the amount of ozone associated with individual stratospheric intrusions by summing up the ozone contained inside the green ozone trace contours (e.g., Figures 3c and 3d) subject to the constraint that the contours must reside in one of two regions (calculated separately), which we refer to hereafter as the North American region (235°–290°E) and the Pacific Basin and North American region (150°–290°). We refer to the ozone intrusion mass contained inside the green contours (divided by the 1979–2015 mean) as *IntrMass*.

We also explored three alternate methods of calculating ozone intrusion mass to test the sensitivity of our *RzvrMass*–*IntrMass* correlations to changes in our detection algorithm thresholds. In the first alternate method, the amount of ozone inside the PV boundaries detected by our algorithm (e.g., red contours in Figure 3) was used as the measure of ozone intrusion mass. This method resulted in notably reduced *RzvrMass*–*IntrMass* correlations, though the correlations were still significant at least at the 95% and 85% levels for ERA-Interim and MERRA-2, respectively. The reduced correlation strength for this method is mostly due to the PV contour boundaries “missing” enough ozone to degrade the calculation. To try to address the ozone missed by the PV contours (and to test the sensitivity of our results to the choice of the ozone detection threshold given to our intrusion algorithm), we also lowered the ozone detection threshold from the 95th percentile value of  $5.1 \times 10^{-7}$  mass mixing ratio to a much lower value of  $4.25 \times 10^{-7}$  mass mixing ratio. By lowering the threshold, a bit more ozone was captured for a few years (e.g., in Figure 3c the green contours more closely matched the red PV contours), but most years remained virtually unchanged (e.g., Figure 3d was essentially unchanged). Lowering the threshold decreased the *RzvrMass*–*IntrMass* correlation strength slightly (0.64 versus 0.77 for ERA-Interim), but the results remained highly significant.

For the final alternate method, the amount of ozone inside the PV boundaries was again calculated, but then the resulting sum was divided by the longitudinal cross-sectional “area” spanned by the PV intrusion boundaries. This second method yields the amount of ozone per PV intrusion unit area and is essentially a measure of ozone intrusion “efficiency.” The result for the final method had significant correlations similar to our primary 95th percentile of ozone threshold method. Because all of the methods produced qualitatively consistent results, we only present results for the *IntrMass* calculation described above that utilizes the 95th percentile ozone threshold for intrusion detection.

We also ran additional tests to verify the robustness of our 330 K isentropic surface results by applying our algorithm along the 315 K isentropic surface. For example, when we applied our algorithm to ERA-Interim ozone along the 315 K surface at 40°N with a ozone threshold value of  $3.15 \times 10^{-7}$  mass mixing ratio, we identify the same set of intrusions compared to our 330 K results but with a *RzvrMass*–*IntrMass* correlation of 0.6 (versus 0.77 for 330 K) at far above the 95% significance level.

The correlations between *IntrMass* and *RzvrMass* presented in section 3.1 are slightly stronger for ERA-Interim than for MERRA-2 data. As we discuss in section A2, these differences are likely a function of the limitations inherent in our ozone intrusion detection algorithm rather than differences in the yearly variability in *IntrMass* between the two reanalyses data sets.



### 2.3. NAM and ENSO Indices

We construct our NAM index time series by subtracting daily climatological geopotential heights from daily geopotential heights, where the daily climatology is obtained by averaging the full 37 year data set into a single 365 day time series and then retaining only the first three annual harmonics. We then integrate the resulting anomaly time series over the polar cap (latitude area weighted  $65^{\circ}$ – $90^{\circ}$ N) and normalize by one STD of the final polar cap average. This calculation was chosen because it minimizes differences associated with using different reanalysis (Cohen et al., 2002; Martineau & Son, 2010) while maintaining a very high correlation ( $\sim 0.96$ ) with the empirical orthogonal function (EOF)-based approach (Baldwin & Thompson, 2009). We use two different NAM pressure “levels” for our correlation calculations. For winter season stratosphere-related NAM variability we use the NAM index pressure weight averaged between 5 and 10 hPa.

The 5–10 hPa pressure region was selected because the NAM-IntrMass correlations peaked at these levels for both reanalyses. In particular, the NAM-IntrMass correlations (section 3.1.1) for ERA-Interim peak when the NAM is calculated in the lower stratosphere, while the MERRA-2 correlations peak when the NAM is calculated in the middle to upper stratosphere, though all levels of NAM calculation nevertheless yielded correlations that were qualitatively consistent and significant for both reanalyses. It is unclear what the cause of these differences are, but one likely possibility is that the two reanalyses simulate the residual circulation and horizontal mixing components along the shallow and deep branches of the BDC in slightly different manners. For spring season UTLS jet-related variability we use the 200 hPa NAM index.

In section 3.1.1 we consider the winter season, time-summed stratospheric NAM index as a predictor for IntrMass in spring. The number of days that the NAM index is summed over is varied from 1 month (1 March to 31 March) to the entire extended winter (1 October to 31 March). To begin, we pressure weight average 6-hourly values of the NAM index between 5 and 10 hPa. We then sum up the resulting pressure-weighted index between a given date, say day “ $X$ ,” and 31 March. Day  $X$  is varied between 1 October and 1 March, and the calculation is repeated for every year (1980–2015). For example, to calculate the 5–10 hPa “time-summed NAM index” for 1980, we sum the 5–10 hPa NAM index between  $X = 1$  October 1979 and 31 March 1980, followed by  $X = 2$  October 1979 to 31 March 1980, and so on until the last value is calculated between  $X = 1$  March and 31 March 1980. This calculation yields a set of values for every day between 1 October and 1 March for each year. In section 3.2 we consider the correlation between the intrusion season (AMJ) 200 hPa NAM index and IntrMass. For this calculation, we simply sum up the 200 hPa NAM index between 1 April and 30 June for each year. Thus, for the 5–10 hPa pressure-averaged “level” we obtain index values for every day in extended winter for every year (1979–2015), while for the spring 200 hPa level we obtain only one value for every year (1979–2015). For brevity and clarity, we refer to the stratospheric time-summed 5–10 hPa pressure-averaged indices and the UTLS time-summed 200 hPa level index as  $\text{NAM}_{\text{winter}}^{\text{Strat}}$  and  $\text{NAM}_{\text{spring}}^{\text{UTLS}}$  respectively.

For ENSO-based indices, we utilize the NOAA Oceanic Niño Index (ONI) (NOAA Center for Weather and Climate Prediction, 2015), which is a 3 month running mean index (i.e., each index value is a 3 month mean; e.g., DJF and JFM). When considering the effect of winter season ENSO forcing on the richness of the spring LMS ozone reservoir (i.e., ENSO planetary wave forcing via the BDC), we average the ONI over the extended winter season (OND, NDJ, DJF, JFM, and FMA) to create one index value for each year 1979–2015; we refer to this index as  $\text{ENSO}_{\text{winter}}$ . When considering the effect of spring season ENSO forcing on the UTLS jet, we average the ONI over the spring season (MAM and AMJ) to create one index value for each year 1979–2015; we refer to this index as  $\text{ENSO}_{\text{spring}}$ . We explored neglecting some ONI periods at the beginning and the end of the winter and spring seasons when creating  $\text{ENSO}_{\text{winter}}$  and  $\text{ENSO}_{\text{spring}}$ , but found the results to be qualitatively equivalent.

### 2.4. Modes of Variability of Zonal Wind

Empirical orthogonal functions (EOFs) of zonal wind on the 350 K isentropic surface were calculated using ERA-Interim data between  $10^{\circ}$ – $70^{\circ}$ N and  $125^{\circ}$ – $270^{\circ}$ E for April and May. This region was chosen because the jet variability that controls intrusion variability over North America has its primary center of action upstream of North America in the jet exit region over the Pacific (e.g., Škerlak et al., 2014). The EOF patterns we show are robust to any reasonable choice for the Asia-Pacific-North American region but do get weaker if June data are included. Before computing the EOFs, we removed the first three annual harmonics of the 1979–2015 daily climatology, cosine latitude weighted and time averaged the resulting data between 1 April and 31 May for each year (1979–2015) and then detrended the resulting data. Because the North et al. (1982) EOF sampling error estimation test indicates that the first two EOFs have the potential to be degenerate, we conducted two additional statistical resampling tests (the jackknife and bootstrap methods; e.g., Wilks, 2011) to verify that the

**Table 2**

April–June IntrMass Versus March RzvrMass Correlation Coefficients for North America (235°–290°E) and the Pacific Basin and North America (150°–290°E) for ERA-Interim and MERRA-2 When All Years Are Included in the Calculation (0 STD), When Only Years Where RzvrMass Is >0.5 STD From the 1979–2015 Climatology, and When RzvrMass Is >1 STD From the 1979–2015 Climatology

Region	0 STD		0.5 STD		1 STD	
	ERA-Interim	MERRA-2	ERA-Interim	MERRA-2	ERA-Interim	MERRA-2
North America	0.77	0.61	0.8	0.85	0.87	0.98
Pacific Basin-North America	0.67	0.68	0.7	0.79	0.88	0.92

Note. All correlations are significant at greater than the 95% level.

first two EOFs represent distinct statistical modes of variability. Hereafter we refer to the first and second EOFs and principal component time series as EOF1, EOF2, PC1, and PC2, respectively. The EOF patterns shown in our results are created by regressing the original data onto the individual PC time series and normalizing so that the units are in  $\text{m s}^{-1}$ .

In the first test (see above), we resample the EOF data without replacement (i.e., the jackknife method). This test yielded a mean spatial correlation of 0.99 (0.5 STD) between the original and resampled EOF1 patterns and a mean variance explained of 30.5% (1% STD) among the EOF1 jackknife realizations; likewise, a mean spatial correlation of 0.98 (0.3 STD) and a mean variance explained of 18.7% (0.5% STD) were obtained for the EOF2 jackknife realizations. A second, 1,000 iteration bootstrap test (resampling with replacement) reveals similar results. We therefore assume that the first two EOFs are robust and represent relatively independent physical features.

### 3. Processes Controlling Stratosphere-to-Troposphere Ozone Transport

The following sections assess how internal dynamic variability and key modes of low-frequency variability combine to cause variations in STT of ozone via stratospheric ozone reservoir variability (StratVarO<sub>3</sub>) versus

jet variability (JetVar). A brief description of the indices used in this analysis is shown in Table 1. We report correlations as significant if their significance level (SL) is  $\geq 95\%$  (i.e., the  $p$  value of the correlation is  $< 0.05$ ); for reference we provide a listing of all SLs for the various index correlations in Tables 2 and 3.

#### 3.1. Stratospheric Reservoir Variability—StratVarO<sub>3</sub>

To gain a general picture of the relationship between winter/spring ozone abundances in the LMS and the amount of ozone contained in AMJ stratospheric intrusions, Figure 4a shows the correlation between IntrMass and a running mean time window of RzvrMass. The running reservoir mean is computed by summing ozone inside the boundaries of our reservoir proxy for 30 day time periods where the central dates of the 30 day windows span 1 January to 31 May. IntrMass is computed for North America as described in section 2.1.

ERA-Interim and MERRA-2 yield qualitatively equivalent pictures of the relationship, with significant correlations generally peaking between late March and early April (Figure 4a), though the ERA-Interim correlation peak (0.8, SL>95%) occurs slightly earlier than the MERRA-2 peak (0.71, SL>95%). The spring peak in the correlation between IntrMass and RzvrMass coincides with the yearly peak (March) in extratropical column ozone (e.g., Figure 1 of Fioletov & Shepherd, 2003) and is therefore consistent with the hypothesis that IntrMass is strongly governed by the richness of the stratospheric ozone reservoir. Although the peak correlation occurs in April, there is still significant information inherent in the reservoir by late February in both reanalyses. This suggests that March is a reasonable time period to use for our ozone reservoir proxy.

**Table 3**

Pairs of Variables (Left Column) and Their Correlation Coefficients (Right Two Columns in Bold Text) for ERA-Interim and MERRA-2 With Significance Levels in Parentheses

Correlation variables		ERA-Interim	MERRA-2
<i>Winter season</i>			
RzvrMass	– IntrMass	<b>0.77</b> (>95%)	<b>0.61</b> (>95%)
NAM <sup>Strat</sup> <sub>winter</sub>	– IntrMass	<b>0.38</b> (>95%)	<b>0.29</b> (>90%)
ENSO <sub>winter</sub>	– RzvrMass	<b>–0.06</b> (24%)	<b>0.09</b> (41%)
<i>Spring season</i>			
NAM <sup>UTLS</sup> <sub>spring</sub>	– IntrMass	<b>0.12</b> (51%)	<b>–0.05</b> (22%)
ENSO <sub>spring</sub>	– IntrMass	<b>–0.19</b> (73%)	<b>0.36</b> (>95%)
PC1	– IntrMass	<b>0.22</b> (82%)	<b>0.34</b> (>95%)
PC2	– IntrMass	<b>–0.15</b> (65%)	<b>0.13</b> (54%)
PC1	– NAM <sup>UTLS</sup> <sub>spring</sub>	<b>0.13</b> (55%)	–
PC2	– NAM <sup>UTLS</sup> <sub>spring</sub>	<b>–0.23</b> (82%)	–
PC1	– ENSO <sub>spring</sub>	<b>0.43</b> (>95%)	–
PC2	– ENSO <sub>spring</sub>	<b>0.76</b> (>95%)	–

Note. RzvrMass refers to the 1–31 March time period, and IntrMass refers to the ozone intrusion mass for North America as defined in section 2.1. The NAM<sup>Strat</sup><sub>winter</sub> correlations represent the peak values as shown in Figure 5a (i.e., time summed for November–March). The bottom four MERRA-2 entries are blank because we only computed EOF versus NAM/ENSO correlations for ERA-Interim (see section 2 for details). The remaining variables use their standard values as defined in the previous sections.

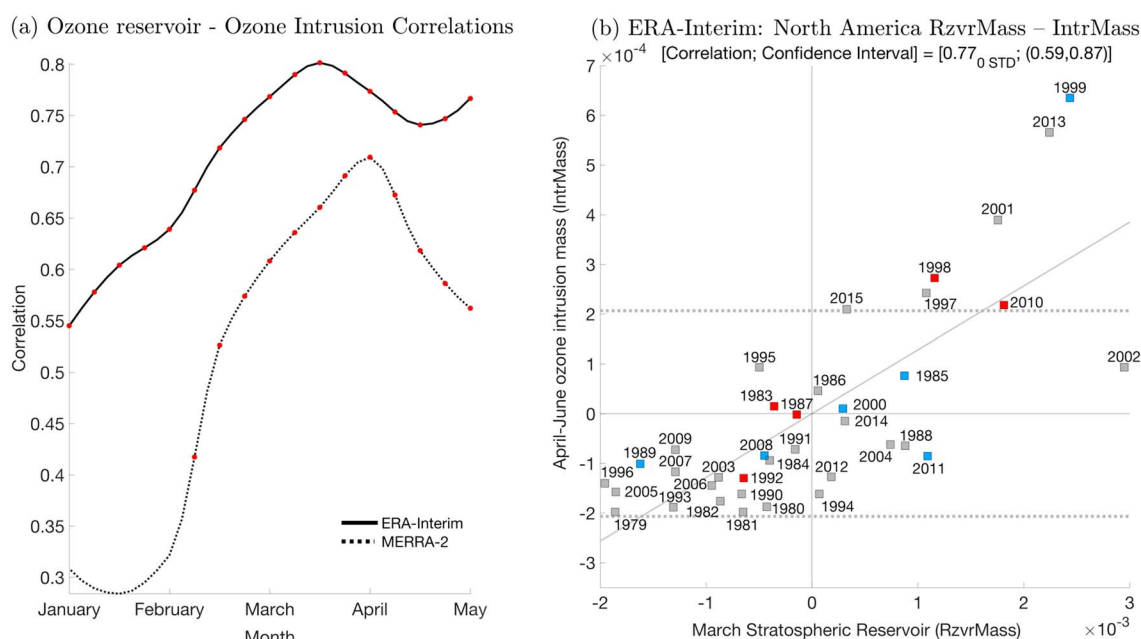


**Figure 4.** (a) Correlations between one month time windows of the 350 K isentropic surface ozone reservoir proxy (RzvrMass) and AMJ ozone intrusion mass (IntrMass) for North America for ERA-Interim (black solid line) and MERRA-2 (black dotted line) on the 330 K isentropic surface; red dots overlaying the lines denote correlations that exceed the 95% significant level. (b) Scatterplot of the yearly (1979–2015) March RzvrMass versus AMJ IntrMass for North America. Red- and blue-filled boxes correspond to years where the ONI index for the combined ENSO<sub>winter</sub> and ENSO<sub>spring</sub> periods (i.e., OND–AMJ) is greater or less than, respectively, 1 STD (0.7358). In Figure 4b, the horizontal gray lines correspond to the  $\pm 1$  STD IntrMass limits. All units are mass mixing ratio.

The relationship between the March RzvrMass and AMJ IntrMass is strong and significant for both North America (235°–290°E, Figure 4b) and the combined Pacific Basin and North America (150°–290°E, not shown). This relationship is even stronger when considering particularly ozone-rich or ozone-poor reservoir years. Table 2 shows the RzvrMass versus IntrMass correlations for ERA-Interim and MERRA-2 (for both IntrMass summation regions) for all years and for years that are only included in the correlation calculation if RzvrMass exceeds various STD thresholds. For example, the ERA-Interim 0 STD RzvrMass threshold correlations for North America correspond to Figure 4b, while the RzvrMass 0.5 STD correlations in Table 2 correspond to the years in Figure 4b that lie to the left or right of approximately  $\pm 0.6 \times 10^{-3}$  on the horizontal (RzvrMass) axis. For the remainder of the manuscript we primarily focus on the North American region, but the results for the combined North America and Pacific Basin are qualitatively similar.

Figure 4b and Table 2 suggest that simply knowing the state of the March ozone reservoir (or even the small latitude-longitude slice that we use as a reservoir proxy, RzvrMass) provides significant information regarding the amount of ozone that will be folded into the troposphere over the course of the following months (AMJ); this highlights the importance of StratVarO<sub>3</sub>. What is not clear, however, is whether low-frequency variability like ENSO and the NAM is related to ozone intrusion mass via either reservoir variability (StratVarO<sub>3</sub>) or UTLS jet variability (JetVar). For example, at first glance there does not appear to be a particularly strong connection between ENSO years and intrusion mass as shown by the blue and red-filled boxes, respectively, in Figure 4b, where ENSO years are defined here as years where the ONI index for the combined ENSO<sub>winter</sub> and ENSO<sub>spring</sub> periods (i.e., OND–AMJ) is greater than 1 STD beyond the 1979–2015 mean. The remaining sections explore how strongly, if at all, ENSO and the NAM are connected to the amount of ozone contained in spring intrusions via StratVarO<sub>3</sub> and JetVar.

### 3.1.1. Modulations of StratVarO<sub>3</sub> by the Winter Season NAM

We consider the possibility that the NAM is related to the richness of the spring ozone reservoir based upon the hypothesis that a stronger (more positive) stratospheric NAM is generally indicative of weaker planetary wave driving, and hence, a weaker residual circulation along the deep branch of the BDC that leads to (1) lower ozone abundances due to weaker poleward and downward ozone transport along the deep branch of the BDC (Figure 1a) and (2) weaker adiabatic heating, lower temperatures, and thus a higher probability for chemical ozone loss (though as discussed in section A1, chemical loss likely has a minor impact on the ozone reservoir).

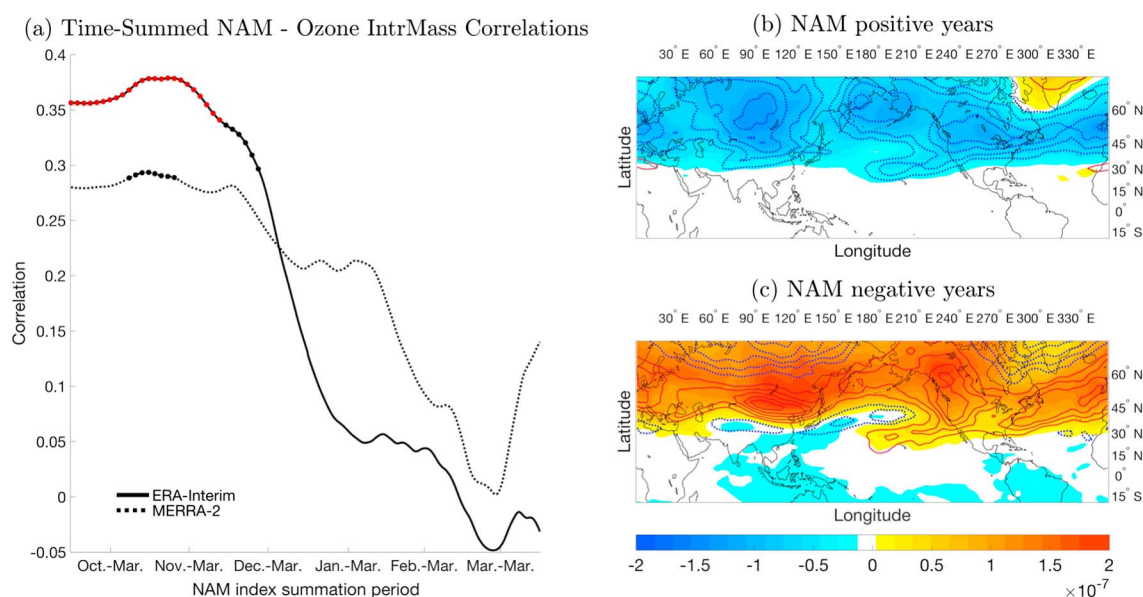


**Figure 5.** (a) Correlations between AMJ IntrMass on the 330 K isentropic surface and the NAM<sup>Strat</sup><sub>winter</sub> index time-summed between 1 October to 1 March for ERA-Interim (black solid line) and MERRA-2 (black dotted line). Black and red dots overlaying all lines in Figure 5a denote correlations that exceed the 90% and 95% significance levels, respectively. The labels on the horizontal axis in Figure 5a correspond to dates over which the NAM indices are summed. For example, October–March indicates that the NAM index was summed between October and March, while March–March indicates that the NAM index was summed between 1 March 1 and 31 March. (b) NAM positive and (c) NAM negative March time mean ozone anomalies for  $\pm 0.5$  STD deviation 1 November to 31 March 31 NAM index summations on the 350 K surface. In Figures 5b and 5c, the filled color contours are ERA-Interim and the solid red and blue dashed contours are positive and negative, respectively, MERRA-2 anomaly contours. The units of Figures 5b and 5c are mass mixing ratio where the color bar corresponds to ERA-Interim, and the  $-1.5 \times 10^{-7}$  to  $1.5 \times 10^{-7}$  isolines in  $0.15 \times 10^{-7}$  increments are shown for MERRA-2.

The converse of this chain of reasoning—that a weaker NAM should lead to higher abundances—should also hold true.

A nontrivial complication to the above line of reasoning is that the role of horizontal mixing—which depending on the local meridional gradient in ozone in which the mixing occurs—can introduce relatively ozone-rich or ozone-poor air from low to high latitudes (e.g., Hegglin & Shepherd, 2007). In particular, along the deep branch above approximately 30 hPa, the meridional ozone gradient is negative (Figure 1a), so quasi-isentropic mixing typically transports ozone-rich air poleward. Below 30 hPa on the other hand (which includes the shallow branch of the BDC), the meridional ozone gradient is positive and quasi-isentropic mixing typically transports ozone-poor air poleward. Thus, the extent to which the NAM is more strongly associated with upper stratospheric horizontal mixing and high-latitude downward residual transport versus lower stratospheric horizontal mixing will determine the validity of the hypothesis stated in the previous paragraph.

These complications notwithstanding, Kieseewetter et al. (2010) provided evidence in support of the NAM downward transport connection on an episodic basis whereby strong positive/negative NAM anomalies were followed by significant downward propagating negative/positive ozone anomalies (see also, Zhang et al., 2017). If each winter season is assumed to be made up of several episodic events, then years when the NAM is weak (or strong)—in a season-long integrated sense—should be associated with a higher (or lower) than average accumulation of ozone in the March lower stratospheric reservoir; this in turn may translate to higher or lower ozone IntrMass. Thus, here we test whether the winter, time-summed strength of the stratospheric NAM (i.e., NAM<sup>Strat</sup><sub>winter</sub>, section 2.3) provides information regarding the strength of ozone intrusions later in the year.

We correlate NAM<sup>Strat</sup><sub>winter</sub> for each time (October–March) of every year (1980–2015) with the total AMJ IntrMass for the North American region for the corresponding years. Figure 5a shows the ERA-Interim and MERRA-2 correlations for IntrMass–NAM<sup>Strat</sup><sub>winter</sub>, which peak at 0.38 and 0.29, respectively. Using other stratospheric pressure level choices for NAM<sup>Strat</sup><sub>winter</sub>—both individually and as pressure-weighted averages—yields similar peak correlations between 0.25 and 0.45 for NAM summation start dates in November (i.e., summing the NAM between mid-November and 31 March) that in general remained statistically significant above the 90% level



until the start dates of the summation calculation reach mid-December. Correlating  $NAM_{winter}^{Strat}$  to  $RzvrMass$  yields similar correlations, except that the  $NAM_{winter}^{Strat}$ - $RzvrMass$  correlation remains statistically significant at the 95% level for shorter time windows than the  $NAM_{winter}^{Strat}$ - $IntrMass$  correlation. For example, the ERA-Interim  $NAM_{winter}^{Strat}$ - $IntrMass$  correlation is significant for windows as short as November–March (Figure 5a), while  $NAM_{winter}^{Strat}$ - $RzvrMass$  remains significant for December–March (not shown). It is likely that this calculation quantifies how successive winter season downward propagating ozone anomalies—which are likely just anomalous accelerations or decelerations in BDC-related downward ozone transport—modulate the strength of subsequent spring season ozone intrusions. The link between the two phenomena is manifest as the richness of the March ozone reservoir.

To see this, Figures 5b and 5c show March ozone anomalies on the 350 K isentropic surface for particularly positive or negative, respectively,  $NAM_{winter}^{Strat}$  years. These anomalies were created by taking the 1 November to 31 March  $NAM_{winter}^{Strat}$  summation for each year 1980–2015, and if any given year's November–March  $NAM_{winter}^{Strat}$  sum was greater than  $\pm 0.5$  of a STD from the 1980–2015 mean, then that year's March time mean ozone on the 350 K isentrope was included in the negative or positive NAM ozone anomaly, respectively. Despite having different model chemistry, different data assimilation schemes, and assimilating different sets of ozone satellite products, both ERA-Interim (filled contours in Figures 5b and 5c) and MERRA-2 (solid and dashed contour lines in Figures 5b and 5c) yield remarkably similar ozone anomaly patterns, except at very high latitudes during NAM negative years. The anomaly patterns are significant for essentially the entire region between  $40^\circ$  and  $70^\circ$ N, which essentially spans the largest anomaly patterns and includes the reservoir proxy ( $RzvrMass$ ) that we outlined in section 2.1.

It should be kept in mind that simply because the correlations in Figure 5 peak for initial summation dates in October to November does not necessarily imply that anomalies that occur late in the winter season are unimportant. For example, while 2001 had minimal ozone anomaly activity in November or December, there was a significant downward propagating ozone anomaly that began descending in late January to early February (see Figure 7 in Kiesewetter et al., 2010), which likely contributed to the high abundance of ozone in the March reservoir (Figure 4b). Still, Figure 5a does imply that *on average*, the dynamic variability—and associated downward ozone transport—that occurs between November and early January is important enough that failing to account for it misses dynamical information needed to explain the state of the ozone reservoir at the end of March. This last point is not completely unexpected because depending on the initial height of the downward propagating ozone anomaly, it generally takes 60–120 days for the anomaly to arrive in the LMS (Kiesewetter et al., 2010); this means that anomalies triggered in late February and beyond may not “arrive” in the LMS in time to modulate the amount of ozone contained in intrusions during peak season (AMJ). We contrast the role of winter season NAM-related transport with the role of ENSO next.

### 3.1.2. Modulations of StratVarO<sub>3</sub> by Winter Season ENSO

Like the NAM, ENSO is thought to drive variability in the BDC and thus changes in STT of ozone (e.g., Neu et al., 2014). To examine the possibility that North American STT variability occurs via StratVarO<sub>3</sub>, Figures 6a and 6b show March time mean ozone anomalies from climatology (1979–2015) for El Niño and La Niña years on the 350 K isentropic surface. March time means are included when the ENSO<sub>winter</sub> index (section 2.3) is greater than one STD from the 1979–2015 mean; this yields 1983, 1987, 1992, 1995, 1998, 2003, and 2010 for El Niño years and 1985, 1989, 1996, 1999, 2000, 2008, 2011, and 2012 for La Niña years. Including all years in the composite weakens the coherence of the pattern shown, which is reflected in the strength of the correlations discussed below.

ERA-Interim and MERRA-2 agree remarkably well for El Niño years (Figure 6a) and are in excellent agreement with GEOSCCM and MLS sensitivity experiments along the 150 hPa surface conducted by Oman et al. (2013) (see their Figure 6). The agreement between the two reanalyses is also reasonable for La Niña years (Figure 6b), though the total anomaly pattern in the extratropics generally appears less coherent for both ERA-Interim and MERRA-2, and MERRA-2 shows a negative anomaly over northern Canada versus the weak but positive anomaly for ERA-Interim. Both reanalyses exhibit dipole patterns over the subtropical central to eastern Pacific that are consistent with previous studies examining the effect of ENSO on winter season stratosphere-troposphere exchange (Scott & Cammas, 2002; Waugh & Polvani, 2000). Specifically, Figure 6a dipole pattern is associated with the anomalously strong and southward shifted subtropical jet that typically occurs during El Niño years, which leads to less extratropical-to-tropical Rossby wave activity (Matthews & Kiladis, 1999) and a consequent lack of equatorward transport of ozone-rich air across the dynamical tropopause; the opposite pattern occurs for La Niña years.

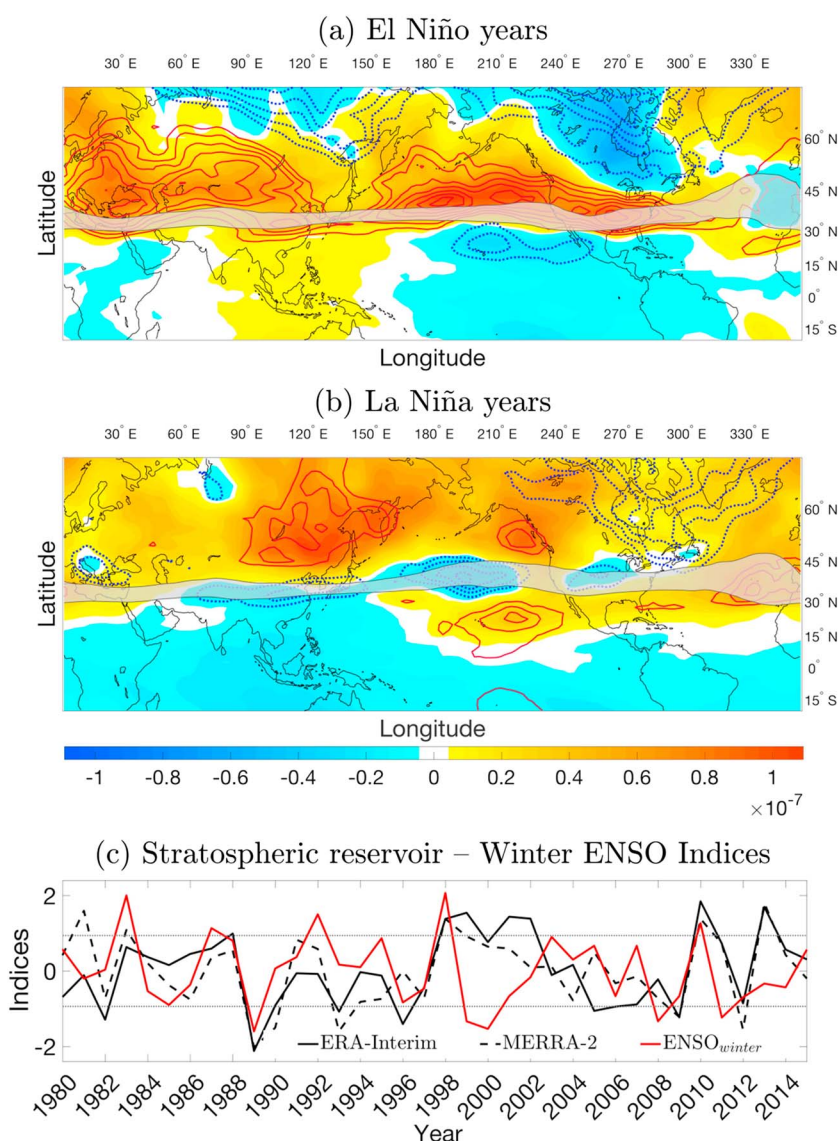


**Figure 6.** March time mean ozone anomalies on the 350 K surface for greater than 1 STD winter season (a) El Niño and (b) La Niña years for ERA-Interim (filled contours) and MERRA-2 (red solid and blue dashed contours for positive and negative values, respectively); for reference, the gray opaque areas enclose the March time mean ERA-Interim 2–4 PVU dynamical tropopause region that correspond to the respective ENSO years shown. In Figures 6a and 6b, the color bar units (ERA-Interim) are mass mixing ratio, and the red solid and blue dashed contours (MERRA-2) correspond to  $-1.5$  to  $1.5$  mass mixing ratio isolines in  $0.1$  increments. (c) Time series of the ERA-Interim RzvMass index (black line), MERRA-2 RzvMass index (black dashed line), and ENSO<sub>winter</sub> index (red line). In Figure 6c, the RzvMass indices have been normalized by their respective STDs so that the indices can be easily compared to the ENSO<sub>winter</sub> index values.

In the following, we correlate ENSO<sub>winter</sub> with RzvMass rather than correlating ENSO<sub>winter</sub> directly with IntrMass; this is done in an attempt to isolate StratVarO<sub>3</sub> versus JetVar-related IntrMass variability in light of the seasonal persistence of ENSO. That is, because ENSO generally persists from winter into spring, directly correlating ENSO<sub>winter</sub> with spring IntrMass may conflate IntrMass variability due to stratospheric reservoir variability (StratVarO<sub>3</sub>) with IntrMass variability that is actually due to jet variability (JetVar) later in the season. On the other hand, if ENSO<sub>winter</sub> modulates IntrMass via StratVarO<sub>3</sub>, then the modulation must occur via RzvMass. Demonstrating a correlation (or not) between ENSO<sub>winter</sub> and RzvMass therefore provides the minimum level of evidence that must exist for there to be a connection between ENSO and IntrMass via StratVarO<sub>3</sub>.

In terms of StratVarO<sub>3</sub>, there is essentially no correlation ( $<0.1$ ) between ENSO<sub>winter</sub> and our RzvMass index for either reanalyses, which is likely due to a combination of factors, including the relatively weak and same signed

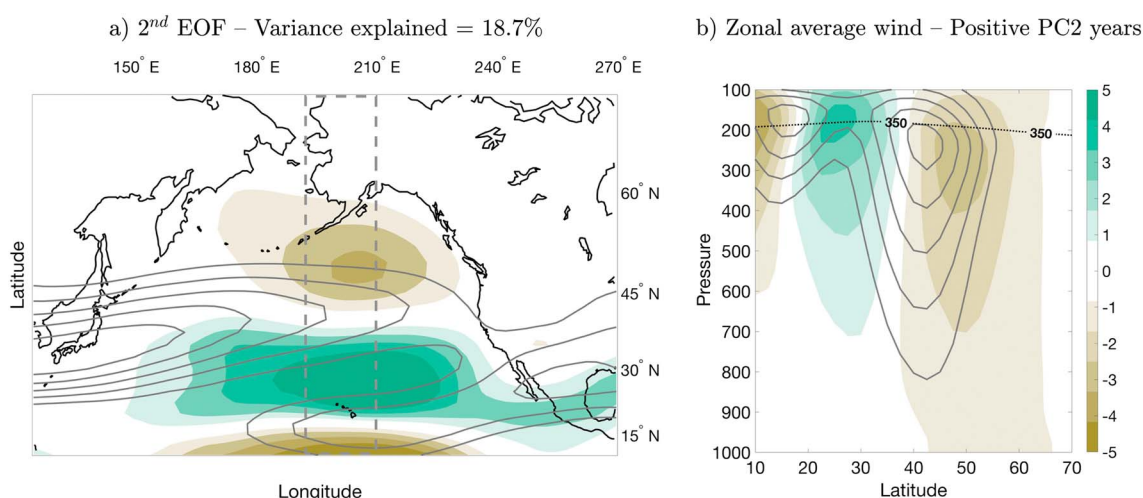


**Figure 7.** (a) Zonal wind anomaly pattern of EOF2 (original data regressed onto PC2; colored contours) and April–May climatological (1979–2015) zonal winds (gray contours) on the 350 K surface. (b) Latitude–height cross section of zonal average (190°–210°E) wind based on EOF2 (colored contours) and April–May climatological (1979–2015) zonal average wind (gray contours). The gray dashed line box in Figure 7a corresponds to the latitude–longitude region used to create the zonal average wind cross section shown in Figure 7b. In Figure 7b, the black dotted line corresponds to the April–May average 350 K isentropic surface on which Figure 7a is plotted. All plots use ERA-Interim data and have units of  $\text{m s}^{-1}$ ; the gray climatological winds are plotted for 20 to 45  $\text{m s}^{-1}$  isolines in 4  $\text{m s}^{-1}$  increments.

anomaly pattern for both ENSO phases and the lack of zonal uniformity in the sign of the anomalies within the 55°–60°N and 150°–290°E RzvMass region. Indeed, if the bounds of RzvMass are shifted to 40°–45°N between 150° and 240°E where the ENSO pattern is more distinct, then the ENSO<sub>winter</sub> versus RzvMass correlation (Figure 6c) becomes 0.31 (94% SL) for MERRA-2 and 0.19 (not significant) for ERA-Interim. If only years when ENSO<sub>winter</sub> is greater than 1 STD from the mean (i.e., the years used in the Figures 6a and 6b composites, see also dashed lines in Figure 6c), then the ENSO<sub>winter</sub>–RzvMass correlation for MERRA-2 rises to 0.57 (92% SL), while ERA-Interim remains insignificant. Thus, while the MERRA-2 and ERA-Interim RzvMasses are significantly correlated (0.72 at >95% SL, c.f. the black dashed and solid lines in Figure 6c), MERRA-2 appears to have a more robust ENSO signal in terms of ozone in the LMS compared to ERA-Interim.

These results suggest that the overall relationship between winter season ENSO and spring IntrMass via StratVarO<sub>3</sub> is not robust. In combination, the data set-dependent correlations, lack of asymmetry in the sign of the ozone anomalies for El Niño versus La Niña, and the spatial nonuniformity in the ENSO-related LMS ozone abundances may help explain why some studies have been able to find a connection between ENSO, stratospheric variability, and IntrMass, while other studies have not.

### 3.2. Jet Variability—JetVar

To examine the role of jet and wave breaking variability (JetVar) for modulating IntrMass over the Pacific–North American region, we compare empirical orthogonal functions (EOFs) of zonal wind to composites of zonal wind on the 350 K surface for years with anomalously strong/weak IntrMass. As discussed in section 2.4, the EOF analysis reveals two leading modes, each of which describes a particular mode of Pacific jet and storm track variability. We begin by considering the structure of the “typical” ENSO teleconnection pattern, which is well captured by EOF2.

The typical warm ENSO teleconnection pattern includes a dipole wind anomaly (negative to the north and positive to the south) with a center of action located toward the jet exit region between 180° and 240°E and with the southern (positive) anomaly having a tongue extending slightly south and eastward across the southern United States and northern Mexico. A similar but opposite signed pattern emerges for La Niña years. There is a strong positive correlation between the PC2 time series and the ENSO<sub>spring</sub> time series (0.76, >99% SL), and the warm ENSO features are easily recognized by comparing the EOF2 wind regression (Figure 7a) to the ENSO wind patterns shown in Figures 1b and 1c, all of which compare well with the larger sample size of ENSO years shown in Chapter 10 of Rasmusson (1991) or Figure 3 of Ji et al. (2016).

However, PC2 is not systematically correlated with IntrMass for ERA-Interim or MERRA-2: ERA-Interim is negatively correlated (−0.15), while MERRA-2 is positively correlated (0.13), both being well below the 95% SL.

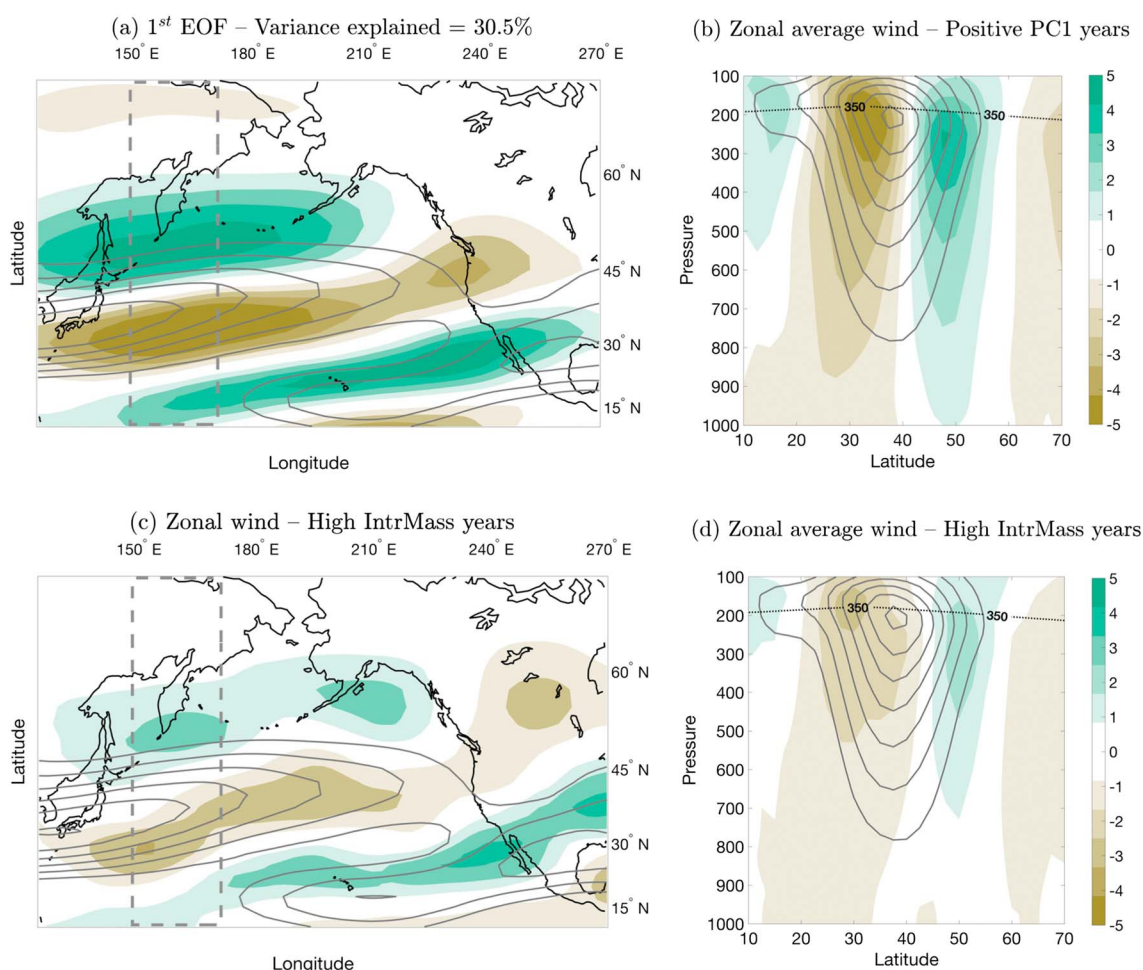


**Figure 8.** (a) Zonal wind anomaly pattern of EOF1 (original data regressed onto PC1; colored contours) and April–May climatological (1979–2015) zonal winds (gray contours) on the 350 K surface. (b) Latitude–height cross section of zonal average (150°–170°E) wind based on EOF1 (colored contours) and April–May climatological (1979–2015) zonal average wind (gray contours). (c) Zonal wind anomaly pattern (colored contours) composited for years when ERA-Interim IntrMass is greater than 0.5 STD of the 1979–2015 mean; the April–May climatological (1979–2015) zonal wind (gray contours) is overlaid. (d) Latitude–height cross section of zonal average (150°–170°E) corresponding to the wind time periods plotted in Figure 8c, with April–May climatological (1979–2015) zonal average winds (gray contours) overlaid. The gray dashed line boxes in Figures 8a and 8c outline the 150°–170°E by 10°–70°N region used in the latitude–height wind cross-section plots shown in Figures 8b and 8d, respectively. In Figures 8b and 8d, the black dotted lines denote the April–May average 350 K isentropic surface that Figures 8a and 8c are plotted on. All plots use ERA-Interim data and have units of  $\text{m s}^{-1}$ ; the gray climatological winds are plotted for 20 to 45  $\text{m s}^{-1}$  isolines in 4  $\text{m s}^{-1}$  increments.

Thus, while some La Niña years are associated with above average IntrMass (e.g., 1985, 1999, and 2000; see Figure 4b), when the whole time record is taken into account, there does not appear to be a strong connection between the typical ENSO teleconnection pattern and IntrMass over North America. However, this does not mean that jet variability is unrelated to yearly variations in IntrMass.

The 350 K isentropic surface EOF1 wind regression (Figure 8a) and the corresponding latitude–height zonal wind cross section for the longitudinal mean between 150° and 170°E (Figure 8b) show a northward shift in the core of the subtropical jet that extends into at least the midtroposphere. A remarkably similar set of wind patterns are obtained by compositing zonal wind on the 350 K isentropic surface for years that had IntrMass sums that were greater than  $\pm 0.5$  STD from climatology (i.e., years in Figure 4b that are above/below approximately  $\pm 1 \times 10^{-4}$  IntrMass mass mixing ratio, respectively). Figures 8c and 8d show the positive 0.5 STD patterns, which are comparable to Figures 8a and 8b. The high correspondence between the wind patterns of EOF1 and the high IntrMass years wind composite is verified by the high linear pattern correlation (0.8) between the colored contour patterns of Figures 8a and 8c. A qualitatively equivalent, but opposite signed, set of patterns result for the negative 0.5 STD IntrMass years.



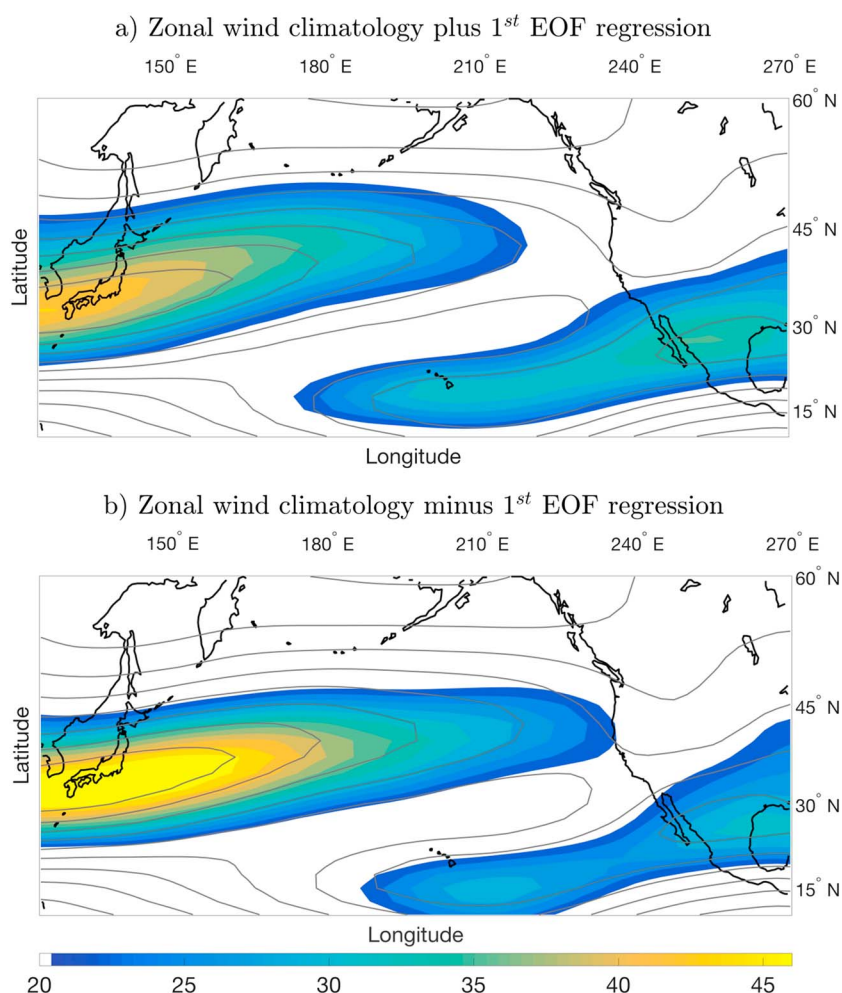


**Figure 9.** (a) April–May (1979–2015) climatological zonal wind plus EOF1 zonal wind regression (filled contours) and (b) April–May (1979–2015) climatological zonal wind minus EOF1 zonal wind regression (filled contours) on the 350 K surface. The gray lines in both panels denote the April–May (1979–2015) climatological zonal wind. All units are in  $\text{m s}^{-1}$ , and both plots use ERA-Interim data.

Adding or subtracting the EOF1 wind regression pattern to the April–May climatology (Figures 9a and 9b, respectively) helps clarify that the dipole anomaly pattern not only represents a jet shift but also represents an extension of the jet and a change in the strength of the jet core. That is, when the PC1 time series is positive, the jet shifts poleward, is retracted westward, and weakens, while the jet shifts southward, extends eastward, and strengthens during time periods when PC1 is negative. This is precisely the wind pattern that Homeyer and Bowman (2013) cite as indicative of time periods of active versus inactive (Figures 9a and 9b, respectively) poleward wave breaking for the March–May time period over the Pacific or Atlantic basins (see their Figure 14).

Some support for the connection between the EOF1 wind pattern, active poleward wave breaking, and the amount of IntrMass is provided by considering the time series of PC1 and IntrMass. The PC1 time series and the North American IntrMass time series are positively correlated for both ERA-Interim (correlation of 0.22, SL = 82%) and MERRA-2 (correlation of 0.34, SL > 95%). While these correlations are not particularly convincing on their own, when taken in combination with the nearly identical wind anomaly patterns that are derived via independent calculations (Figures 8a and 8c), the correlation and wind anomaly results suggest that the changes in the structure of the subtropical jet—which are indicative of anomalies in the frequency of wave breaking—occur in conjunction with at least a subset of the high or low IntrMass years over western North America.

The logical next question is whether this type of jet variability can be related to modes of low-frequency variability such as the NAM or ENSO. In terms of the NAM, we find no significant relationship between the spring season time-summed UTLS NAM index ( $NAM_{spring}^{UTLS}$ ) and PC1, PC2, or IntrMass for either reanalysis data set. This suggests that NAM-related wind variability via JetVar does not systematically modulate IntrMass variability over the Pacific-North American region during late spring.

Similar to our earlier  $ENSO_{winter}$  results, we find a significant  $ENSO_{spring}$ -IntrMass relationship for MERRA-2 (0.36) but not for ERA-Interim. However, we cannot rule out the possibility that this correlation is actually just a manifestation of RzvrMass variability because the same ENSO phase typically persists from winter into spring, and as discussed in section 3.1.2,  $ENSO_{winter}$ , RzvrMass, and IntrMass are also positively correlated. That said, there is reason to believe that some of the  $ENSO_{spring}$ -IntrMass relationship is specifically related to JetVar. Indeed,  $ENSO_{spring}$  is significantly correlated with PC1 (0.43), and in turn, PC1 is significantly correlated with IntrMass (0.34). At this point it is unclear why MERRA-2 reveals a significant correlation between ENSO and IntrMass via both StratVarO<sub>3</sub> and JetVar, while ERA-Interim does not.

It is important to note that the positive correlation between PC1,  $ENSO_{spring}$ , and IntrMass means that high IntrMass years are associated with a northward shift in the jet during El Niño and vice versa for La Niña, which is opposite to the typical ENSO teleconnection pattern. Specifically, the center of action of the EOF1 dipole is located much farther west compared to the typical ENSO teleconnection pattern (150°–180°E for EOF1 instead of 180°–240°E for EOF2). Second, the EOF1 southern dipole anomaly has a northward and eastward extension instead of a southward and eastward extension. And finally, and perhaps most importantly, the sign of the dipole pattern is opposite to the typical ENSO teleconnection pattern. Thus, while ENSO may turn out to be related to spring IntrMass over North America via JetVar, it appears to do so via wind variability that is related to north Pacific wave breaking frequency rather than typical east Pacific ENSO teleconnection patterns. Indeed, both reanalysis data sets support the notion that wave breaking frequency is related to IntrMass via JetVar, while only MERRA-2 supports that notion JetVar is modulated by ENSO. We suggest two possible explanations for our ENSO-JetVar results in section 4.

#### 4. Conclusions

Stratospheric intrusions are an important contributor to North American background (NAB) ozone levels during boreal spring (e.g., Langford et al., 2016; Lin et al., 2015). However, a conclusive accounting of the relative importance of stratospheric versus tropospheric low-frequency variability for modulating the strength and frequency of stratospheric ozone intrusions has to date remained elusive. To address this uncertainty, we have compared the relative importance of the NAM and ENSO—in both the stratosphere (winter) and troposphere (spring)—in the context of two physical mechanisms (Figure 1) that modulate STT of ozone on interannual timescales, namely, (1) StratVarO<sub>3</sub>, which corresponds to variability in the richness of the spring-time stratospheric ozone reservoir that governs the amount of ozone contained per stratospheric intrusion and (2) JetVar, which corresponds to Pacific jet variability that governs the frequency and location of stratospheric intrusions. Using two reanalysis data sets (ERA-Interim and MERRA-2), we have shown which forms of low-frequency variability robustly modulate STT of ozone via these two mechanisms and which forms do not.

Specifically, based on the relative strength of the correlations between ozone intrusion mass (IntrMass) and the StratVarO<sub>3</sub> versus JetVar indices (Table 3), our results suggest that StratVarO<sub>3</sub> likely exerts a stronger governing influence on April–June STT of ozone over North America than does JetVar. In particular, the relationships between IntrMass and both stratospheric ozone reservoir mass (RzvrMass) and the winter season, stratospheric portion of the NAM, are strong, statistically significant, and consistent for both reanalyses. In contrast, the IntrMass-JetVar and IntrMass-ENSO relationships are weaker in terms of correlation strength, statistical significance, and the consistency of the relationship between the two reanalyses.

Regarding the NAM, we find that the extended winter season (November–March) time-summed strength of the stratospheric portion of the NAM ( $NAM_{winter}^{Strat}$ ) is significantly correlated with IntrMass in the subsequent late spring season (StratVarO<sub>3</sub>). This result supports the notion that anomalous stratospheric NAM events—especially when they occur repeatedly within one season—are associated with anomalous high-latitude BDC transport (Kiesewetter et al., 2010) that increases the amount of ozone in the LMS reservoir (Figure 1a). That said, the winter of 2009 provides a cautionary example. While 2009 included a record breaking NAM event in the form of a major SSW, there were nevertheless anomalously low abundances of ozone in the extratropical LMS (Figure A1). A possible interpretation of this finding is that winters with steady and

strong wave driving—which is indicative of a weak NAM—but without a strong SSW may well be the most conducive to building up an ozone-rich LMS reservoir and subsequently large STT of ozone (StratVarO<sub>3</sub>). It is worth noting that other forms of interannual stratospheric variability (e.g., QBO, Neu et al., 2014) also imply a connection to IntrMass via StratVarO<sub>3</sub>.

In terms of IntrMass variability via JetVar on the other hand, we find no relationship between jet shifts associated with the time-summed spring season UTLS NAM (NAM<sup>UTLS<sub>spring</sub></sup>) and IntrMass variability. This is dynamically consistent with Ogi et al. (2004) who find very weak NAM-related storm track variability during boreal summer over the North Pacific-North American region.

The role of ENSO is also difficult to untangle. Generally speaking, MERRA-2 implies that ENSO is related to IntrMass variability, while ERA-Interim does not. Thus, in terms of ENSO-related variability, it is difficult to know whether the difference in the results between data sets is due to the limited time period of the data record, deficiencies in reanalysis-based ENSO variability, or whether the physical relationships are simply weak and insignificant. For example, we find a relatively weak and reanalysis-dependent connection between winter season ENSO and spring IntrMass via StratVarO<sub>3</sub>. Likewise, while our results confirm that some La Niña years are consistent with northward jet shifts that may have contributed to increased STT of ozone over North America (e.g., 1985 and 1999, Figures 4b and 7a), that same teleconnection expectation may not be enough to overcome an ozone-poor stratospheric reservoir during other years (e.g., 1989 and 2008, Figure 4b). Indeed, we find no significant correlation between the typical ENSO teleconnection pattern (Figure 7a) and IntrMass over North America for either reanalyses (PC2-IntrMass in Table 3) when considering the entire data record (1979–2015). Interestingly, this result offers a rather different view on the connection between STT of ozone and ENSO compared to the results of Lin et al. (2015), though it should be kept in mind that our results did not analyze variability in the vertical depth of stratospheric intrusions. We do, however, find a connection between IntrMass over North America and a different manifestation of subtropical jet variability (JetVar), which may be weakly modulated by ENSO consistent with the findings of Langford et al. (1998).

Our results suggest that the JetVar-IntrMass connection (i.e., the EOF PC1 versus IntrMass correlation) is more consistent with wave breaking frequency over the North Pacific (c.f., Figure 9 and Figure 14 of Homeyer & Bowman, 2013) than it is with changes in East Pacific teleconnection patterns that are typically associated with ENSO. Both reanalyses reveal a consistent relationship, but again, the MERRA-2 results are more statistically significant. However, by building UTLS Pacific jet composites based on high/low IntrMass years that compare very well with our EOF1 wind regressions (Figure 8), we are able to provide independent support for the importance of the EOF1 type of jet variability.

In particular, we find that the relevant type of jet variability is manifest as north or south shifts in the latitude of the jet (Figure 8b) that are accompanied by weakening and westward retraction or strengthening and eastward extension, respectively, of the jet core (Figure 9). Our results indicate that the northward shifted and westward retracted phase of this pattern is positively correlated with El Niño (PC1-ENSO<sub>spring</sub> in Table 3), which means that the phase of the wind pattern is opposite in sign to the typical ENSO teleconnection pattern (e.g., Ji et al., 2016). However, our results leave unclear whether the EOF1-type jet variability that we have isolated is a result of some form of northwest Pacific teleconnection variability or whether the jet shifts are simply the configuration that results from time periods with a higher than average frequency of wave breaking due to random internal dynamic variability (or a mixture of both). Whatever the explanation turns out to be, it must be able to account for the fact that ENSO appears to be correlated with a jet regime (Figure 8a) that is opposite in sign and is shifted westward compared to the typical ENSO jet pattern (Figure 7a). We suggest two possible explanations that are consistent with this jet regime, one related to teleconnection variability and one related to wave breaking frequency.

One possible explanation involves the fact that spring is a transition period in terms of the location of where the greatest sensitivity for the Rossby response (i.e., teleconnection pattern) relevant to North America resides (Newman & Sardeshmukh, 1998). During winter, the Rossby response relevant to North America is most sensitive to divergence forcing in the eastern Pacific, which is consistent with the excitation of the typical ENSO teleconnection pattern (c.f. our Figure 7a to Figure 3a of Ji et al., 2016). However, by late spring the most sensitive region for a Rossby response relevant to North America shifts to the western Pacific and the sensitivity to smaller-scale forcing such as the Madden-Julian oscillation (MJO) increases. Given that the MJO is known to be sensitive to ENSO basic states in the tropics (Chi-Yung & Ngar-Cheung, 2005; Hendon et al., 2007; Hsu & Xiao, 2016; Kessler, 2001; Liu et al., 2016; Pohl & Matthews, 2007), then it may be possible that ENSO modulates

the strength of the MJO as it propagates through the western Pacific where the MJO convective divergence field triggers an efficient Rossby response (Moon et al., 2011).

A second possible explanation is related to the frequency of poleward cyclonic wave breaking (LC2, Thorncroft et al., 1993). Shapiro et al. (2001) and Scott and Cammas (2002) find that El Niño conditions are associated with an increased frequency of poleward LC2-type wave breaking. Homeyer and Bowman (2013) find that enhanced poleward wave breaking between March and May is associated with a wind pattern nearly identical to the wind pattern we show for years when PC1 is positive (Figure 9). Given that we find this wind pattern to be positively correlated with both El Niño and anomalously high IntrMass over North America, then it stands to reason that ENSO may modulate the frequency of poleward wave breaking in the North Pacific and hence the frequency of ozone intrusions over North America.

Unfortunately, one difficulty that arises when trying to determine the root cause of the connection of ENSO to North American ozone intrusion variability is related to the fact that the same phase of ENSO generally persists from winter into spring. Thus, given that the warm (cold) phase of ENSO modulates both StratVarO<sub>3</sub> and JetVar in ways that tend to increase (decrease) IntrMass, it is unclear from our results which is more important, ENSO's affect on IntrMass via StratVarO<sub>3</sub> or via JetVar. Nevertheless, our results illustrate that the most anomalous years for ozone intrusions over the western United States likely arise from a combination of interannual variability of the ozone reservoir combined with variations in the Pacific jet stream that may arise from a multitude of possibilities (e.g., ENSO, the MJO, and random internal variability).

Several potential limitations concerning our intrusion detection methods and choice of data should be mentioned. While previous authors (e.g., Morgenstern & Carver, 2001) have used methodologies similar to our intrusion detection algorithm for measuring STT of ozone, it should be noted that our method does not formally measure irreversible ozone transport. Thus, future work will need to carefully determine whether the IntrMass variability that we have isolated and quantified is fully representative of variability in irreversible STT of ozone.

A second limitation inherent in this work relates to our choice of data. Connecting interannual variability of stratospheric ozone to variability in STT of ozone requires a data product that can be used to quantify the amount of ozone inside the vertically thin structures of both the LMS ozone reservoir and individual intrusion filaments in a globally gridded fashion. This means that long-term data record total column ozone products are insufficient, yet the relatively short data record of vertically resolved products (e.g., MLS: 2005-present) are, at least at this point, too short to draw firm mechanistic conclusions.

Climate model and reanalysis data on the other hand present their own set of difficulties. For example, deficiencies in model transport associated with the BDC may lead to inaccuracies in extratropical stratospheric ozone during winter and spring (e.g., Donner et al., 2011; Lin & Fu, 2013), while a lack of adequate model physics (e.g., no tropospheric dry deposition in ERA-Interim or MERRA-2) or inadequate model resolution (Ott et al., 2016) can lead to inaccuracies in measuring the true amount of ozone contained in stratospheric intrusions that reach the planetary boundary layer. Highlighting these difficulties is not meant as a criticism of any particular experimental approach (model experiments, reanalysis data, or otherwise), but the difficulties do serve as a reminder that drawing too firm of a conclusion using one single approach can potentially misrepresent the importance of any single physical mechanism that modulates STT of ozone on interannual timescales. For example, while our RzvrMass-IntrMass and NAM-IntrMass correlations are suggestive of the controlling influence of the time-integrated BDC on STT of ozone during spring, our analysis approach did not formally connect variations in the strength of the BDC along its two branches to variations in STT of ozone. Indeed, more work is needed in this particular area especially given the differing conclusions found by Neu et al. (2014) versus Hsu and Prather (2014) regarding the connection between the interannual variability of the BDC and STT of ozone.

With these difficulties in mind, we chose to use reanalysis data because its long-term, globally gridded nature allowed us to detect and catalog a significant sample size of stratospheric intrusions and quantify the relationship between the frequency and strength of those intrusions and the richness of the spring stratospheric ozone reservoir and jet variability. While reanalysis data are likely insufficient for drawing firm conclusions regarding ozone in the lowermost troposphere or the planetary boundary layer, reanalyses do simulate the interannual variability of ozone in the stratosphere and upper troposphere with sufficient fidelity



(see Appendix A and Wargan et al., 2017) that valuable conclusions can be drawn regarding the connection between low-frequency variability and North American background (NAB) ozone levels.

Still, despite the above uncertainties, our results firmly demonstrate that the richness of the LMS ozone reservoir in early spring—regardless of the processes that led to its current abundance—is an extremely strong indicator for the amount of ozone that will be injected downward into the troposphere during the ensuing late spring. Thus, unlike wave breaking frequency or jet stream shifts due to either the NAM or ENSO that can be difficult to accurately predict months in advance, useful information regarding future STT of ozone can be ascertained at any given time during late winter simply by measuring the current state of ozone in the LMS.

## Appendix A: Data Validation

### A1. Ozone Reservoir

Approximately 80% of middle- to high-latitude interannual stratospheric column ozone variability is associated with wave-driven variations in the strength of the BDC, with the remaining 20% due to changes associated with chemistry (Fusco & Salby, 1999; Salby & Callaghan, 2002; Weber et al., 2011). Stratospheric planetary wave driving peaks in NH winter (Charney & Drazin, 1961; Randel et al., 2002), and there is a strong subtropical transport barrier (Haynes & Shuckburgh, 2000; Shuckburgh et al., 2009); collectively, this causes the deep branch of the BDC to dominate over the shallow branch of the BDC, which in turn leads to a seasonal buildup of ozone in the LMS toward the beginning of spring (Konopka et al., 2015; Ploeger & Birner, 2016; Ray et al., 1999). As spring progresses into summer, stratospheric wave driving and the subtropical transport barrier weaken and the springtime seasonal peak of ozone in the LMS ozone reservoir (Figure 1a) begins to decline. This summer “flushing” of the March ozone reservoir (Bönisch et al., 2009; Hegglin & Shepherd, 2007) corresponds with the late spring peak in stratosphere-to-troposphere ozone transport over western North America (James et al., 2003; Lefohn et al., 2001; Škerlak et al., 2014; Terao et al., 2008). In terms of chemical processes, springtime heterogeneous losses occur primarily above the 400 K isentropic surface (e.g., Livesey et al., 2015; Manney et al., 2011) and thus even substantial springtime losses are unlikely to significantly impact the amount ozone in the LMS.

Taking all of these dynamical and chemical processes into account, it is fair to presume that March reservoir anomalies are largely dictated by the strength of the BDC in the immediately prior winter months, with perhaps some additional amount of variability due to loss of ozone to the troposphere due to STT of ozone during the concurrent winter season and longer timescale anomaly residuals left in the system from the previous year (e.g., Fioletov & Shepherd, 2003; Tegtmeier et al., 2010; Weber et al., 2011; Zhang et al., 2017). Given that the interannual variability of the BDC is reasonably well simulated in modern reanalyses (Abalos et al., 2015), then collectively, the above line of reasoning suggests that reanalyses should be adequate for measuring interannual March ozone reservoir anomalies. To help verify this supposition, we have compared ozone reservoir calculations for Aura MLS to the same calculations using ERA-Interim and MERRA-2 (Figure A1).

Aura MLS ozone is assimilated into ERA-Interim in 2008, the second half of 2009, and 2010–2015, while it is assimilated into MERRA-2 for 2005–2015. ERA-Interim therefore provides a somewhat independent estimate of the richness of the spring ozone reservoir for 4 of the 11 MLS years. We use MLS version 4 data (Livesey et al., 2017), which has 2–3 km resolution in the UTLS. The MLS data are prepared by taking cosine square weighted, 24 h averages around each gridpoint, and then averaging each day's gridded data over the month. The data are then interpolated onto isentropic surfaces using MERRA-2 temperatures. Comparing March mean ozone on the 350 K isentrope for ERA-Interim (Figures A1a and A1b), MLS (Figures A1c and A1d), and MERRA-2 (Figures A1e and A1f) reveals that all three data sets exhibit low ozone abundances in 2009 and high abundances in 2011. These 2 years were chosen because they demonstrate two key features (one dynamical and one chemical) related to the strength of the spring reservoir that both reanalyses were able to reproduce.

First, winters with persistently negative NAM states (i.e., weak vortex states) are typically associated with rich spring ozone reservoirs and consequently large STT of ozone in the ensuing late spring and summer months (section 3; see also Kieseewetter et al., 2010). However, while the winter of 2009 was punctuated by one of the strongest negative NAM events on record (Martineau & Son, 2010), all three data sets indicate that the spring reservoir was ozone poor. Interestingly, ERA-Interim reproduces the anomalously weak 2009 ozone abundances just as well as MERRA-2 (Figure A1g) despite not assimilating MLS ozone during the winter and spring of 2009; this suggests that reanalysis products are able to reproduce the sign of reservoir anomalies with or without the assimilation of vertically resolved MLS data. The ozone-poor 2009 spring also provides

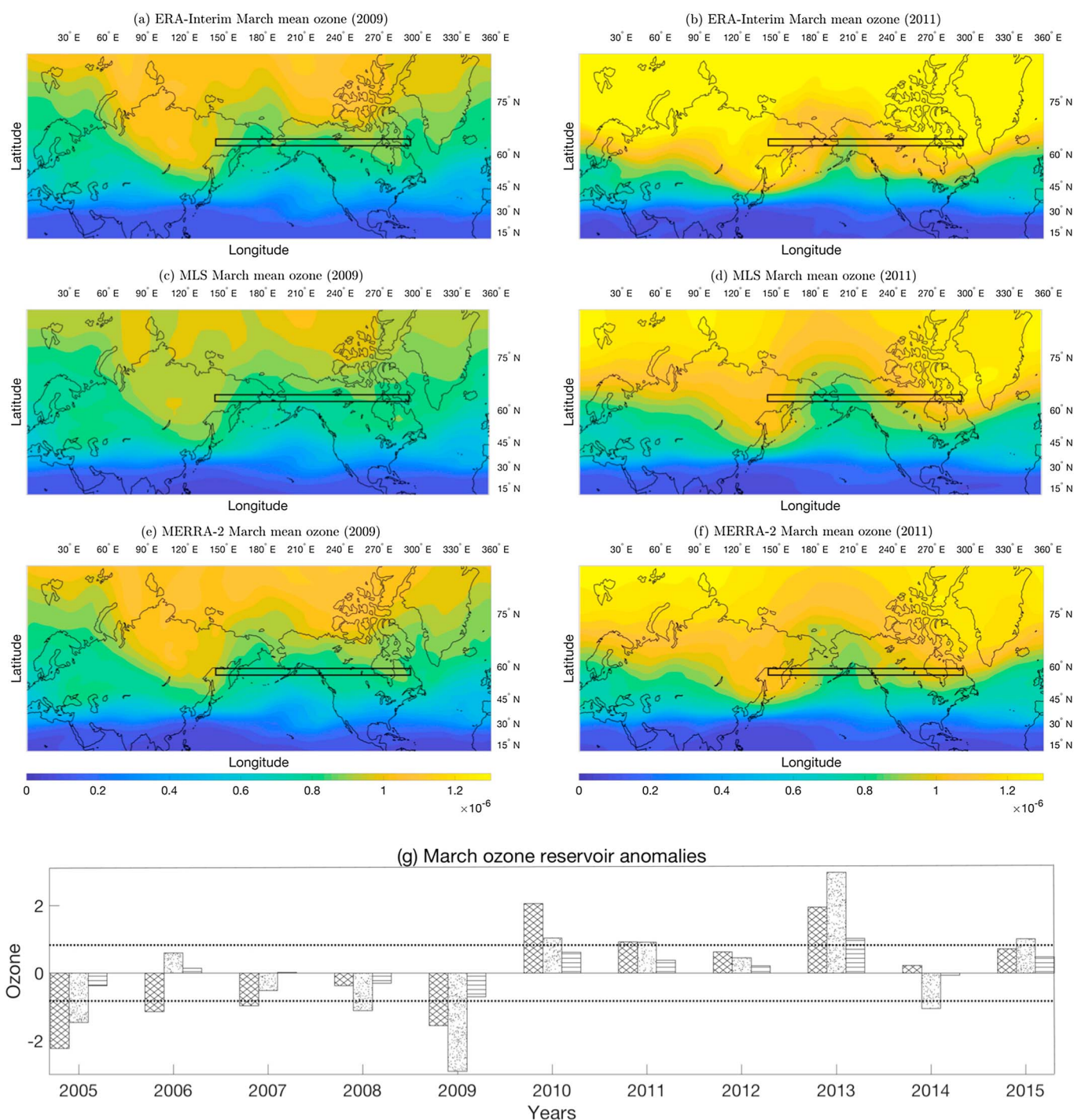


**Figure A1.** Figures A1a–A1f are March mean ozone on the 350 K isentropic surface for 2009 (Figures A1a, A1c, and A1e) and 2011 (Figures A1b, A1d, and A1f) for (a, b) ERA-Interim, (c, d) Aura MLS, and (e, f) MERRA-2. The black boxes overlaying Figures A1a and A1b denote the ozone reservoir proxy boundaries used in the calculations shown in Figure A1g and used throughout the manuscript. (g) 2005–2015 March time mean ozone for the reservoir proxy boundaries depicted by the black boxes in Figures A1a and A1b for ERA-Interim (boxes with cross hatching), Aura MLS (boxes with stippling), and MERRA-2 (boxes with horizontal lines). Units in Figures A1a–A1f are mass mixing ratio; the units in Figure A1g are  $10^{-6}$  mass mixing ratio.

an example of the imperfect correlation between the strength of the winter season NAM and the amount of ozone folded into the troposphere during summer that we present in section 3. Turning our attention to chemical processes, we note that the spring of 2011 provides support for the contention that heterogeneous loss is relatively unimportant in terms of the richness of the spring ozone reservoir because despite having

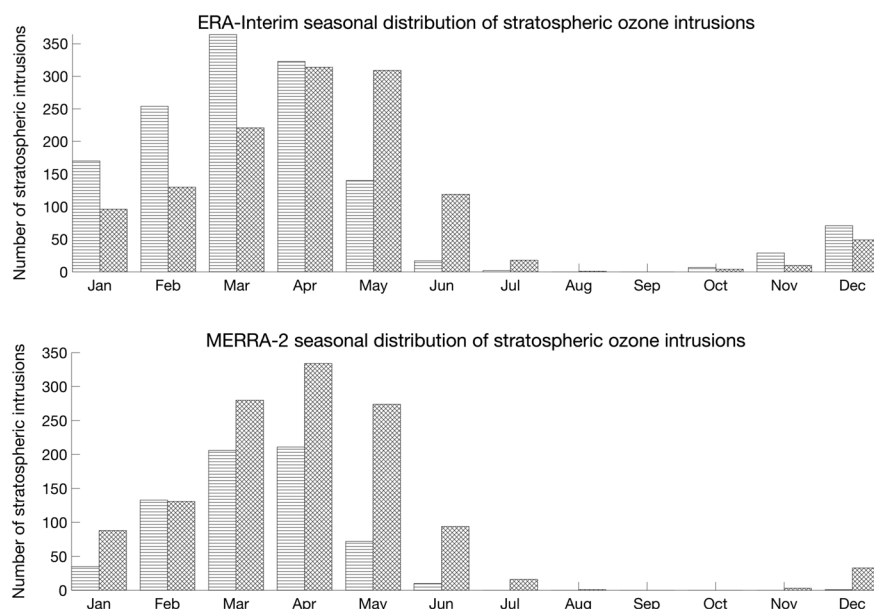


**Figure A2.** Seasonal distribution of ozone intrusions on the 330 K and 350 K isentropic surfaces at 15°N (boxes with cross hatching) and 40°N (boxes with horizontal lines), respectively, for (top) ERA-Interim and (bottom) MERRA-2. The distributions are plotted in terms of the number of intrusions (vertical axis) per month that are isolated by our intrusion detection algorithm. Note that while the number counts of intrusions are somewhat dependent on the threshold criterion (see section 2.2), the seasonal distribution is robust.

the largest heterogeneous loss of ozone on record for the NH (Manney et al., 2011), all three data products confirm that 2011 had an anomalously rich ozone reservoir.

Reservoir anomalies are also fairly consistent for other years in the MLS period and beyond (1980–2015). In general, the agreement between the two reanalyses and MLS is quite good for RzvrMass (Figure A1g), especially for years that had anomalies larger than 0.5 of a STD from climatology (shown as the horizontal dotted lines in Figure A1g). The 2 years that are somewhat inconclusive (2006 and 2014) can be understood in terms of the spatial uniformity (or lack thereof) of the ozone anomalies on the 350 K surface for years with particularly strong (or weak) RzvrMass anomalies. Generally speaking, years with strong RzvrMass anomalies in the LMS are characterized by largely zonally uniform anomaly structures that span large portions of the NH north of the dynamical tropopause (we provide examples for NAM- and ENSO-related anomalies in Section 3). In contrast, 2006 and 2014 had anomaly patterns that were zonally nonuniform (not shown), which translates to higher than average sensitivity in the sign and magnitude of RzvrMass. Nevertheless, years similar to 2006 and 2014 are sufficiently rare that RzvrMass for ERA-Interim and MERRA-2 are highly correlated (0.7 at >95% significance) for the entire 1980–2015 period. This result is broadly consistent with Wargan et al. (2017) who find that MERRA-2 ozone in the UTLS is highly correlated (>0.8) with independent ozonesonde data for the 1991–2012 period.

#### A2. Ozone Intrusions

Reanalysis data should also be sufficient for the purpose of measuring intrusions because once the ozone reservoir is “set” at the end of March, then the long photochemical lifetime of ozone in the UTLS (on the order of weeks to years, e.g., Figure 5.3 in Brasseur & Solomon, 2005) imply that the amount of ozone inside of subsequent AMJ stratospheric intrusions should be relatively accurately represented. To test this assumption, we compared the known seasonal variability of ozone intrusions with the seasonal variability of intrusions detected by our algorithm.

Our algorithm correctly captures the NH wintertime peak of subtropical stratospheric PV intrusions over the Pacific and Atlantic Basins (c.f. Waugh & Polvani, 2000 and Albers et al., 2016), and when the algorithm is applied to ozone on the 330 K and 350 K isentropic surfaces at 40°N and 15°N, respectively; it correctly captures the ozone intrusion peak during spring (Lefohn et al., 2001, 2011; Lin et al., 2012; Olsen et al., 2013) for both ERA-Interim and MERRA-2 (Figure A2). Note that the intrusion counts shown in Figure A2 for the two different isentropic surfaces correspond to somewhat different wave breaking phenomenon. The intrusions

detected along the 350 K isentrope are indicative of vertically shallow—largely isentropic—mixing in the equatorial westerly wind ducts (Albers et al., 2016), while the intrusions along the 330 K isentrope are more typically associated with vertically deep tropopause folds due to extratropical wave breaking (Gettelman et al., 2011).

One minor caveat when using our intrusion detection algorithm is that various modeling platforms simulate mixing processes—including filamentation and transport barriers—slightly differently (Lauritzen et al., 2014). This fact is reflected in the ability of our intrusion detection algorithm to accurately identify all of the filamentary structures and streamers for any single wave breaking/intrusion event. In particular, we find that ozone and PV in the interior of intrusions represented by MERRA-2 (finite volume cube sphere with  $\sim 0.5^\circ$  horizontal resolution) are more filamented when compared to ERA-Interim (spectral Gaussian with  $\sim 0.7^\circ$  horizontal resolution); in practice, this means that our algorithm has a slightly more difficult time identifying the full set of intrusions in MERRA-2 versus ERA-Interim (this is true even though we apply the algorithm to the 2.5° version of the data). This issue is reflected in the slightly weaker—though still highly significant—MERRA-2 correlations in section 3 and the fact that the yearly variability of IntrMass between the two reanalyses is 0.68 (also statistically significant at the 95% level). One way to verify the hypothesis that this is an intrusion detection issue and not an actual ozone budget issue is to use the IntrMass boundaries as detected from ERA-Interim but to use the MERRA-2 ozone field in the IntrMass calculation; when this is done, the correlation between the ERA-Interim and MERRA-2 yearly variability of IntrMass jumps up to 0.99. Thus, any differences between MERRA-2 and ERA-Interim IntrMass are due largely to technical difficulties in intrusion detection rather than in differences in interseasonal ozone variability.

#### Acknowledgments

This work was supported by the NSF Atmospheric and Geospace Science Postdoctoral Fellowship program (J. R. A.) and NASA grant NNX13AM24G (J. R. A. and J. P.). We also thank the NASA GMAO and ECMWF for the reanalysis data and the Aura MLS team for MLS data and computing support. MERRA-2 data were downloaded from <https://disc.sci.gsfc.nasa.gov/daac-bin/FTPSubset2.pl>, and ERA-Interim data were downloaded courtesy of NCAR at <https://rda.ucar.edu/datasets/ds627.0/>.

#### References

- Abalos, M., Legras, B., Ploeger, F., & Randel, W. J. (2015). Evaluating the advective Brewer-Dobson circulation in three reanalyses for the period 1979–2012. *Journal of Geophysical Research: Atmospheres*, 120, 7534–7554. <https://doi.org/10.1002/2015JD023182>
- Albers, J. R., Kiladis, G. N., Birner, T., & Dias, J. (2016). Tropical upper-tropospheric potential vorticity intrusions during sudden stratospheric warmings. *Journal of the Atmospheric Sciences*, 73(6), 2361–2384.
- Ambaum, M. H., & Hoskins, B. J. (2002). The NAO troposphere–stratosphere connection. *Journal of Climate*, 15(14), 1969–1978.
- Baldwin, M. P., & Thompson, D. W. (2009). A critical comparison of stratosphere-troposphere coupling indices. *Quarterly Journal of the Royal Meteorological Society*, 135(644), 1661–1672.
- Bönisch, H., Engel, A., Curtius, J., Birner, T., & Hoor, P. (2009). Quantifying transport into the lowermost stratosphere using simultaneous in-situ measurements of SF-6 and CO-2. *Atmospheric Chemistry and Physics*, 9(16), 5905–5919.
- Bosilovich, M. G., Akella, S., Coy, L., Cullather, R., & Draper, C. (2015). MERRA-2: Initial evaluation of the climate. NASA Tech. Rep. Series on Global Modeling and Data Assimilation (Tech. Rep. NASA/TM-2015-104606, Vol. 39, 136 pp.). Greenbelt, MD: NASA Goddard Space Flight Center.
- Brasseur, G., & Solomon, S. (2005). *Aeronomy of the middle atmosphere: Chemistry and physics of the stratosphere and mesosphere* (3rd ed.). Berlin: Springer.
- Butchart, N. (2014). The Brewer-Dobson circulation. *Reviews of Geophysics*, 52, 157–184. <https://doi.org/10.1002/2013RG000448>
- Charney, J., & Drazin, P. (1961). Propagation of planetary-scale disturbances from the lower into the upper atmosphere. *Journal of Geophysical Research*, 66(1), 83–109.
- Chi-Yung, T., & Ngar-Cheung, L. (2005). Modulation of the Madden-Julian Oscillation by ENSO: Inferences from observations and GCM simulations. *Journal of the Meteorological Society of Japan*, 83(5), 727–743.
- Cohen, J., Salstein, D., & Saito, K. (2002). A dynamical framework to understand and predict the major Northern Hemisphere mode. *Geophysical Research Letters*, 29(10), 1412. <https://doi.org/10.1029/2001GL014117>
- Cooper, O., Stohl, A., Hübner, G., Hsie, E., Parrish, D., Tuck, A., ... Lefohn, A. S. (2005). Direct transport of midlatitude stratospheric ozone into the lower troposphere and marine boundary layer of the tropical Pacific Ocean. *Journal of Geophysical Research*, 110, D23310. <https://doi.org/10.1029/2005JD005783>
- Dee, D. P., Uppala, S., Simmons, A., Berrisford, P., Poli, P., Kobayashi, S., ... Vitart, F. (2011). The ERA-Interim, reanalysis: Configuration and performance of the data assimilation system. *Quarterly Journal of the Royal Meteorological Society*, 137, 553–597.
- Donner, L. J., Wyman, B. L., Hemler, R. S., Horowitz, L. W., Ming, Y., Zhao, M., ... Zeng, F. (2011). The dynamical core, physical parameterizations, and basic simulation characteristics of the atmospheric component AM3 of the GFDL global coupled model CM3. *Journal of Climate*, 24(13), 3484–3519.
- Dragani, R. (2011). On the quality of the ERA-Interim ozone reanalyses: Comparisons with satellite data. *Quarterly Journal of the Royal Meteorological Society*, 137(658), 1312–1326.
- Elbern, H., Hendricks, J., & Ebel, A. (1998). A climatology of tropopause folds by global analyses. *Theoretical and Applied Climatology*, 59(3–4), 181–200.
- Fioletov, V. E., & Shepherd, T. G. (2003). Seasonal persistence of midlatitude total ozone anomalies. *Geophysical Research Letters*, 30(7), 1417. <https://doi.org/10.1029/2002GL016739>
- Fusco, A. C., & Salby, M. L. (1999). Interannual variations of total ozone and their relationship to variations of planetary wave activity. *Journal of Climate*, 12(6), 1619–1629.
- García-Herrera, R., Calvo, N., García, R., & Giorgetta, M. (2006). Propagation of ENSO temperature signals into the middle atmosphere: A comparison of two general circulation models and ERA-40 reanalysis data. *Journal of Geophysical Research*, 111, D06101. <https://doi.org/10.1029/2005JD006061>
- Gelaro, R., McCarty, W., Suárez, M., Todling, R., Molod, A., Tackacs, L., ... Zhao, B. (2017). The Modern-Era Retrospective Analysis for Research and Applications, Version 2 (MERRA-2). *Journal of Climate*, 30, 5419–5454.



- Gettelman, A., Hoor, P., Pan, L., Randel, W., Hegglin, M., & Birner, T. (2011). The extratropical upper troposphere and lower stratosphere. *Reviews of Geophysics*, 49, RG3003. <https://doi.org/10.1029/2011RG000355>
- Global Modeling and Assimilation Office (GMAO) (2015). MERRA-2 inst33dasmNv: 3d, 3-Hourly, Instantaneous, Model-Level, Assimilation, Assimilated Meteorological Fields V5.12.4, Greenbelt, MD, USA, Goddard Earth Sciences Data and Information Services Center (GES DISC). Accessed [2016] <https://doi.org/10.5067/WWQSQX8IVFW8>
- Haynes, P., & Shuckburgh, E. (2000). Effective diffusivity as a diagnostic of atmospheric transport: I. Stratosphere. *Journal of Geophysical Research*, 105(22), 22,777–22,794. <https://doi.org/10.1029/2000JD900093>
- Hegglin, M. I., & Shepherd, T. G. (2007). O<sub>3</sub>-N<sub>2</sub>O correlations from the atmospheric chemistry experiment: Revisiting a diagnostic of transport and chemistry in the stratosphere. *Journal of Geophysical Research*, 112, D19301. <https://doi.org/10.1029/2006JD008281>
- Hendon, H. H., Wheeler, M. C., & Zhang, C. (2007). Seasonal dependence of the mjo–enso relationship. *Journal of Climate*, 20(3), 531–543.
- Hess, P., & Zbinden, R. (2013). Stratospheric impact on tropospheric ozone variability and trends: 1990–2009. *Atmospheric Chemistry and Physics*, 13(2), 649–674.
- Hess, P., Kinnison, D., & Tang, Q. (2015). Ensemble simulations of the role of the stratosphere in the attribution of northern extratropical tropospheric ozone variability. *Atmospheric Chemistry and Physics*, 15(5), 2341–2365.
- Hoerling, M. P., Schaack, T. K., & Lenzen, A. J. (1993). A global analysis of stratospheric-tropospheric exchange during northern winter. *Monthly Weather Review*, 121(1), 162–172.
- Holton, J. R., Haynes, P. H., McIntyre, M. E., Douglass, A. R., Rood, R. B., & Pfister, L. (1995). Stratosphere-troposphere exchange. *Reviews of Geophysics*, 33(4), 403–439.
- Homeyer, C. R., & Bowman, K. P. (2013). Rossby wave breaking and transport between the tropics and extratropics above the subtropical jet. *Journal of the Atmospheric Sciences*, 70(2), 607–626.
- Hoskins, B. J. (1991). Towards a PV- $\theta$  view of the general circulation. *Tellus A*, 43(4), 27–35.
- Hsu, J., & Prather, M. J. (2009). Stratospheric variability and tropospheric ozone. *Journal of Geophysical Research*, 114, D06102. <https://doi.org/10.1029/2008JD010942>
- Hsu, J., & Prather, M. J. (2014). Is the residual vertical velocity a good proxy for stratosphere-troposphere exchange of ozone? *Geophysical Research Letters*, 41, 9024–9032. <https://doi.org/10.1002/2014GL061994>
- Hsu, P.-C., & Xiao, T. (2016). Differences in the initiation and development of Madden-Julian Oscillation over the Indian Ocean associated with two types of El Niño. *Journal of Climate*, 30, 1397–1415.
- James, P., Stohl, A., Forster, C., Eckhardt, S., Seibert, P., & Frank, A. (2003). A 15-year climatology of stratosphere–troposphere exchange with a Lagrangian particle dispersion model 2. Mean climate and seasonal variability. *Journal of Geophysical Research*, 108(D12), 8522. <https://doi.org/10.1029/2002JD002639>
- Ji, X., Neelin, J. D., & Mechoso, C. R. (2016). Baroclinic-to-barotropic pathway in El Niño–Southern Oscillation teleconnections from the viewpoint of a barotropic Rossby wave source. *Journal of the Atmospheric Sciences*, 73(12), 4989–5002.
- Kang, D., Lee, M.-I., Im, J., Kim, D., Kim, H.-M., Kang, H.-S., ... MacLachlan, C. (2014). Prediction of the Arctic Oscillation in boreal winter by dynamical seasonal forecasting systems. *Geophysical Research Letters*, 41, 3577–3585. <https://doi.org/10.1002/2014GL060011>
- Kessler, W. S. (2001). EOF representations of the Madden-Julian Oscillation and its connection with ENSO. *Journal of Climate*, 14(13), 3055–3061.
- Kiesewetter, G., Sinnhuber, B.-M., Vountas, M., Weber, M., & Burrows, J. (2010). A long-term stratospheric ozone data set from assimilation of satellite observations: High-latitude ozone anomalies. *Journal of Geophysical Research*, 115, D10307. <https://doi.org/10.1029/2009JD013362>
- Konopka, P., Ploeger, F., Tao, M., Birner, T., & Riese, M. (2015). Hemispheric asymmetries and seasonality of mean age of air in the lower stratosphere: Deep versus shallow branch of the Brewer-Dobson circulation. *Journal of Geophysical Research: Atmospheres*, 120, 2053–2066. <https://doi.org/10.1002/2014JD022429>
- Lait, L. R. (1994). An alternative form for potential vorticity. *Journal of the Atmospheric Sciences*, 51(12), 1754–1759.
- Lamarque, J.-F., & Hess, P. G. (2004). Arctic Oscillation modulation of the Northern Hemisphere spring tropospheric ozone. *Geophysical Research Letters*, 31, L06127. <https://doi.org/10.1029/2003GL019116>
- Langford, A. (1999). Stratosphere-troposphere exchange at the subtropical jet: Contribution to the tropospheric ozone budget at midlatitudes. *Geophysical Research Letters*, 26(16), 2449–2452.
- Langford, A., & Reid, S. (1998). Dissipation and mixing of a small-scale stratospheric intrusion in the upper troposphere. *Journal of Geophysical Research*, 103(D23), 31,265–31,276.
- Langford, A., O’Leary, T., Masters, C., Aikin, K., & Proffitt, M. (1998). Modulation of middle and upper tropospheric ozone at northern midlatitudes by the El Niño/Southern Oscillation. *Geophysical Research Letters*, 25(14), 2667–2670.
- Langford, A., Aikin, K., Eubank, C., & Williams, E. (2009). Stratospheric contribution to high surface ozone in Colorado during springtime. *Geophysical Research Letters*, 36, L12801. <https://doi.org/10.1029/2009GL038367>
- Langford, A., Brioude, J., Cooper, O., Senff, C., Alvarez, R., Hardesty, R., ... Oltmans, S. (2012). Stratospheric influence on surface ozone in the Los Angeles area during late spring and early summer of 2010. *Journal of Geophysical Research*, 117, D00V06. <https://doi.org/10.1029/2011JD016766>
- Langford, A., Senff, C., Alvarez, R., Brioude, J., Cooper, O., Holloway, J., ... Williams, E. J. (2015). An Overview of the 2013 Las Vegas Ozone Study (LVOS): Impact of stratospheric intrusions and long-range transport on surface air quality. *Atmospheric Environment*, 109, 305–322.
- Langford, A., Alvarez, R., Brioude, J., Fine, R., Gustin, M., Lin, M., ... Williams, E. J. (2016). Entrainment of stratospheric air and Asian pollution by the convective boundary layer in the Southwestern U.S. *Journal of Geophysical Research: Atmospheres*, 122, 1312–1337. <https://doi.org/10.1002/2016JD025987>
- Lauritzen, P., Ullrich, P., Jablonowski, C., Bosler, P., Calhoun, D., Conley, A., ... Tolstykh, M. A. (2014). A standard test case suite for two-dimensional linear transport on the sphere: Results from a collection of state-of-the-art schemes. *Geoscientific Model Development*, 7, 105–145.
- Lefohn, A. S., Oltmans, S. J., Dann, T., & Singh, H. B. (2001). Present-day variability of background ozone in the lower troposphere. *Journal of Geophysical Research*, 106(D9), 9945–9958.
- Lefohn, A. S., Wernli, H., Shadwick, D., Limbach, S., Oltmans, S. J., & Shapiro, M. (2011). The importance of stratospheric–tropospheric transport in affecting surface ozone concentrations in the western and northern tier of the United States. *Atmospheric Environment*, 45(28), 4845–4857.
- Liang, Q., Douglass, A., Duncan, B., Stolarski, R., & Witte, J. (2009). The governing processes and timescales of stratosphere-to-troposphere transport and its contribution to ozone in the Arctic troposphere. *Atmospheric Chemistry and Physics*, 9(9), 3011–3025.

- Lin, M., Fiore, A. M., Cooper, O. R., Horowitz, L. W., Langford, A. O., Levy, H., ... Senff, C. J. (2012). Springtime high surface ozone events over the western United States: Quantifying the role of stratospheric intrusions. *Journal of Geophysical Research*, 117, D00V22. <https://doi.org/10.1029/2012JD018151>
- Lin, M., Fiore, A. M., Horowitz, L. W., Langford, A. O., Oltmans, S. J., Tarasick, D., & Rieder, H. E. (2015). Climate variability modulates western US ozone air quality in spring via deep stratospheric intrusions. *Nature Communications*, 12(6), 7105.
- Lin, P., & Fu, Q. (2013). Changes in various branches of the Brewer–Dobson circulation from an ensemble of chemistry climate models. *Journal of Geophysical Research: Atmospheres*, 118, 73–84. <https://doi.org/10.1029/2012JD018813>
- Liu, F., Li, T., Wang, H., Deng, L., & Zhang, Y. (2016). Modulation of boreal summer intraseasonal oscillations over the western North Pacific by ENSO. *Journal of Climate*, 29(20), 7189–7201.
- Livesey, N., Santee, M., & Manney, G. (2015). A match-based approach to the estimation of polar stratospheric ozone loss using Aura Microwave Limb Sounder observations. *Atmospheric Chemistry and Physics*, 15(17), 9945–9963.
- Livesey, N. J., Read, W. G., Wagner, P. A., Froidevaux, L., Lambert, A., Manney, G. L., ... Martinez, E. (2017). EOS Aura MLS version 4.2x level 2 data quality description document (Tech. Rep. JPL D-33509). Pasadena, CA: NASA Jet Propulsion Laboratory, California Institute of Technology.
- Long, C. S., Fujiwara, M., Davis, S., Mitchell, D. M., & Wright, C. J. (2017). Climatology and interannual variability of dynamic variables in multiple reanalyses evaluated by the SPARC reanalysis intercomparison project (S-RIP). *Atmospheric Chemistry and Physics*, 17, 14,593–14,629. <https://doi.org/10.5194/acp-17-14593-2017>
- Manney, G. L., Santee, M. L., Rex, M., Livesey, N. J., Pitts, M. C., Veefkind, P., ... Zinoviev, N. S. (2011). Unprecedented Arctic ozone loss in 2011. *Nature*, 478(7370), 469–475.
- Martineau, P., & Son, S.-W. (2010). Quality of reanalysis data during stratospheric vortex weakening and intensification events. *Geophysical Research Letters*, 37, L22801. <https://doi.org/10.1029/2010GL045237>
- Matthews, A. J., & Kiladis, G. N. (1999). Interactions between ENSO, transient circulation, and tropical convection over the Pacific. *Journal of Climate*, 12(10), 3062–3086.
- Moon, J.-Y., Wang, B., & Ha, K.-J. (2011). ENSO regulation of MJO teleconnection. *Climate Dynamics*, 37(5–6), 1133–1149.
- Morgenstern, O., & Carver, G. D. (2001). Comparison of cross-tropopause transport and ozone in the upper troposphere and lower stratosphere region. *Journal of Geophysical Research*, 106(10), 10,205–10,221.
- Müller, R., & Günther, G. (2003). A generalized form of Lait's modified potential vorticity. *Journal of the Atmospheric Sciences*, 60(17), 2229–2237.
- Neu, J. L., Flury, T., Manney, G. L., Santee, M. L., Livesey, N. J., & Worden, J. (2014). Tropospheric ozone variations governed by changes in stratospheric circulation. *Nature Geoscience*, 7(5), 340–344.
- Newman, M., & Sardeshmukh, P. D. (1998). The impact of the annual cycle on the North Pacific/North American response to remote low-frequency forcing. *Journal of the Atmospheric Sciences*, 55(8), 1336–1353.
- NOAA Center for Weather and Climate Prediction (2015). NOAA Oceanic Niño Index. College Park, MD: NOAA Center for Weather and Climate Prediction, Climate Prediction Center. Retrieved from <https://www.cpc.ncep.noaa.gov/products/analysismonitoring/ensostuff/ensoyears.shtml>
- North, G. R., Bell, T. L., Cahalan, R. F., & Moeng, F. J. (1982). Sampling errors in the estimation of empirical orthogonal functions. *Monthly Weather Review*, 110(7), 699–706.
- Ogi, M., Yamazaki, K., & Tachibana, Y. (2004). The summertime annular mode in the Northern Hemisphere and its linkage to the winter mode. *Journal of Geophysical Research*, 109, D20114. <https://doi.org/10.1029/2004JD004514>
- Olsen, M. A., Douglass, A. R., & Kaplan, T. B. (2013). Variability of extratropical ozone stratosphere–troposphere exchange using microwave limb sounder observations. *Journal of Geophysical Research: Atmospheres*, 118, 1090–1099. <https://doi.org/10.1029/2012JD018465>
- Olsen, M. A., Wargan, K., & Pawson, S. (2016). Tropospheric column ozone response to ENSO in GEOS-5 assimilation of OMI and MLS ozone data. *Atmospheric Chemistry and Physics*, 16(11), 7091–7103.
- Oman, L. D., Douglass, A. R., Ziemke, J. R., Rodriguez, J. M., Waugh, D. W., & Nielsen, J. E. (2013). The ozone response to ENSO in Aura satellite measurements and a chemistry–climate simulation. *Journal of Geophysical Research: Atmospheres*, 118, 965–976. <https://doi.org/10.1029/2012JD018546>
- Ott, L. E., Duncan, B. N., Thompson, A. M., Diskin, G., Fasnacht, Z., Langford, A. O., ... Yoshida, Y. (2016). Frequency and impact of summertime stratospheric intrusions over Maryland during DISCOVER-AQ (2011): New evidence from NASA's GEOS-5 simulations. *Journal of Geophysical Research: Atmospheres*, 121, 3687–3706. <https://doi.org/10.1002/2015JD024052>
- Pan, L., Solomon, S., Randel, W., Lamarque, J.-F., Hess, P., Gille, J., ... McCormick, M. P. (1997). Hemispheric asymmetries and seasonal variations of the lowermost stratospheric water vapor and ozone derived from SAGE II data. *Journal of Geophysical Research*, 102(D23), 28,177–28,184.
- Ploeger, F., & Birner, T. (2016). Seasonal and inter-annual variability of lower stratospheric age of air spectra. *Atmospheric Chemistry and Physics*, 16(15), 10,195–10,213.
- Pohl, B., & Matthews, A. J. (2007). Observed changes in the lifetime and amplitude of the Madden-Julian Oscillation associated with interannual ENSO sea surface temperature anomalies. *Journal of Climate*, 20(11), 2659–2674.
- Proffitt, M. H., & Langford, A. O. (1997). Ground-based differential absorption lidar system for day or night measurements of ozone throughout the free troposphere. *Applied Optics*, 36(12), 2568–2585.
- Randel, W. J., Wu, F., & Stolarski, R. (2002). Changes in column ozone correlated with the stratospheric EP flux. *Journal of the Meteorological Society of Japan*, 80(4B), 849–862.
- Rasmusson, E. M. (1991). *Teleconnections Linking Worldwide Climate Anomalies* (Vol. 535). New York: Cambridge University Press.
- Ray, E. A., Moore, F. L., Elkins, J. W., Dutton, G. S., Fahey, D. W., Vömel, H., ... Rosenlof, K. H. (1999). Transport into the Northern Hemisphere lowermost stratosphere revealed by in situ tracer measurements. *Journal of Geophysical Research*, 104, 26,565–26,580.
- Rood, R. B., Douglass, A. R., & Cerniglia, M. C. (2000). Seasonal variability of middle-latitude ozone in the lowermost stratosphere derived from probability distribution functions. *Journal of Geophysical Research*, 105(D14), 17–793.
- Salby, M. L., & Callaghan, P. F. (2002). Interannual changes of the stratospheric circulation: Relationship to ozone and tropospheric structure. *Journal of Climate*, 15(24), 3673–3685.
- Scott, R., & Cammas, J. (2002). Wave breaking and mixing at the subtropical tropopause. *Journal of the Atmospheric Sciences*, 59(15), 2347–2361.
- Shapiro, M. (1980). Turbulent mixing within tropopause folds as a mechanism for the exchange of chemical constituents between the stratosphere and troposphere. *Journal of the Atmospheric Sciences*, 37(5), 994–1004.
- Shapiro, M., Wernli, H., Bond, N., & Langland, R. (2001). The influence of the 1997–99 El Niño Southern Oscillation on extratropical baroclinic life cycles over the eastern North Pacific. *Quarterly Journal of the Royal Meteorological Society*, 127(572), 331–342.

- Shepherd, T. G. (2007). Transport in the middle atmosphere. *Journal of the Meteorological Society of Japan*, 85, 165–191.
- Shuckburgh, E., d'Ovidio, F., & Legras, B. (2009). Local mixing events in the upper troposphere and lower stratosphere. Part II: Seasonal and interannual variability. *Journal of the Atmospheric Sciences*, 66(12), 3695–3706.
- Škerlak, B., Sprenger, M., & Wernli, H. (2014). A global climatology of stratosphere–troposphere exchange using the ERA-Interim data set from 1979 to 2011. *Atmospheric Chemistry and Physics*, 14(2), 913–937.
- Škerlak, B., Sprenger, M., Pfahl, S., Tyrlis, E., & Wernli, H. (2015). Tropopause folds in ERA-Interim: Global climatology and relation to extreme weather events. *Journal of Geophysical Research: Atmospheres*, 120, 4860–4877. <https://doi.org/10.1002/2014JD022787>
- Tegtmeier, S., Fioletov, V., & Shepherd, T. (2010). A global picture of the seasonal persistence of stratospheric ozone anomalies. *Journal of Geophysical Research*, 115, D18119. <https://doi.org/10.1029/2009JD013011>
- Terao, Y., Logan, J. A., Douglass, A. R., & Stolarski, R. S. (2008). Contribution of stratospheric ozone to the interannual variability of tropospheric ozone in the northern extratropics. *Journal of Geophysical Research*, 113, D18309. <https://doi.org/10.1029/2008JD009854>
- Thompson, D. W., & Wallace, J. M. (1998). The Arctic Oscillation signature in the wintertime geopotential height and temperature fields. *Geophysical Research Letters*, 25(9), 1297–1300.
- Thorncroft, C., Hoskins, B., & McIntyre, M. (1993). Two paradigms of baroclinic-wave life-cycle behaviour. *Quarterly Journal of the Royal Meteorological Society*, 119(509), 17–55.
- Thorpe, A. J. (1986). Synoptic scale disturbances with circular symmetry. *Monthly Weather Review*, 114(7), 1384–1389.
- Thouret, V., Cammas, J.-P., Sauvage, B., Athier, G., Zbinden, R., Nédélec, P., ... Karcher, F. (2006). Tropopause referenced ozone climatology and inter-annual variability (1994–2003) from the MOZAIC programme. *Atmospheric Chemistry and Physics*, 6(4), 1033–1051.
- Voulgarakis, A., Hadjinicolaou, P., & Pyle, J. (2011). Increases in global tropospheric ozone following an El Niño event: Examining stratospheric ozone variability as a potential driver. *Atmospheric Science Letters*, 12(2), 228–232.
- Wargan, K., Labow, G., Frith, S., Pawson, S., Livesey, N. J., & Partyka, G. (2017). Evaluation of the ozone fields in NASA's MERRA-2 reanalysis. *Journal of Climate*, 30(8), 2961–2988.
- Waugh, D. W., & Polvani, L. M. (2000). Climatology of intrusions into the tropical upper troposphere. *Geophysical Research Letters*, 27(23), 3857–3860.
- Weber, M., Dikty, S., Burrows, J. P., Garny, H., Dameris, M., Kubin, A., ... Langematz, U. (2011). The Brewer-Dobson circulation and total ozone from seasonal to decadal time scales. *Atmospheric Chemistry and Physics*, 11(21), 11,221–11,235.
- Wilks, D. S. (2011). *Statistical methods in the atmospheric sciences* (Vol. 100). Oxford, UK: Academic Press.
- Zeng, G., & Pyle, J. A. (2005). Influence of El Niño Southern Oscillation on stratosphere/troposphere exchange and the global tropospheric ozone budget. *Geophysical Research Letters*, 32, L01814. <https://doi.org/10.1029/2004GL021353>
- Zhang, J., Xie, F., Tian, W., Han, Y., Zhang, K., Qi, Y., ... Shu, J. (2017). Influence of the Arctic Oscillation on the vertical distribution of wintertime ozone in the stratosphere and upper troposphere over Northern Hemisphere, 30(8), 2905–2919.